Anonymous Referee #1

The authors acknowledge the helpful comments and corrections of Referee #1, which helped to improve the quality of the manuscript. Below, each comment is answered point-by-point.

This paper is well written and an interesting contribution to the field. I particularly enjoyed the analysis of TKE and the Brunt-Väisälä frequency, showing that the vertical mixing of the water column is stronger when waves are considered. I therefore recommend it to be published after the following issues are addressed.

Do you think there is any tide included in the results shown in Fig. 5? There appears to be a roughly 12.5 hour period to the oscillation, and this could be dominating the time series and masking the effect of the wind-jet. I know the tide is probably very small in this region, but it should be considered. I suggest you perform a harmonic analysis on the time series (make sure it is long enough) and subtract the tide from the time series, so you are left with a non-tidal residual. If the small changes during the wind-jet you describe are due to the wind-jet, then they should still be there.
Right, the current time series were not filtered and included the tide. We have subtracted the subinertial time series using the same filter we used in a previous study. Figure 5 has been changed and the filter explanation included in the text.

Page 6 Lines 4 – 9: Please state what boundary forcing was imposed on the nested models, i.e. water elevations and/or currents (barotropic / baroclinic), temperature, salinity?
The nesting between each domain consist on providing the boundary spectra from the coarser to the smaller domain. In the article, we only talked about "boundary conditions", now we have rewritten it as "spectra boundary conditions.

The naming of the model runs uncS, cRS and uncR are not well defined. They first appear in Table 1 and are used in a number of the figures. I suggest you define them in the text in the first paragraph in section 3.1. On reading the text it becomes evident what they are/mean but it is confusing at first.
We have added the naming of the model runs at the first paragraph in section 2.3.2, where the system set-up is explained and the three model runs are first mentioned.

In section 3.2 (page 12, line 12) the wind-jet event is said to start at 02:00 UTC, yet Fig. 5 only starts at 03:00. I suggest you start the x-axis at 02:00 to correspond to the text. Also, please label the x-axis in Fig. 5, Time (UTC) or similar.
Right, it has been fixed. Now the Figure starts at 02:00 UTC and the x-axis label has been added.

Minor Comments / Revisions:

Page 1 Line 9: leading a larger mixed-layer depth –> leading to a larger mixed-layer depth
Fixed.

Page 2 Line 29: has been previously –> has previously been
Fixed.

Page 2 Lines 30-31 in the study region and the wind-wave characterization, and water shelf circulation was investigated –> in the study region, and the wind-wave characterization and water shelf circulation were investigated
Fixed.

Page 3 Line 22: data obtained–> data were obtained
Fixed.

Page 3 Line 22: and an high-frequency –> and high-frequency
Fixed.

Page 3 Line 33: KHz –> kHz
Fixed.

Page 4 Line 8: and a two-ways coupling run –> and a model run with two-way coupling
Fixed.

Page 4 Line 11: is N needed?
No, it has been deleted.

Page 9 Line 19: And Fig. 3 –> Fig. 3
Fixed.

Page 12 Line 14: What do you mean by "negative increase" exactly? Does that make it a decrease, or do you mean it becomes more negative. You could say that the magnitude of the current increases. Please rephrase.
Right, this explanation was not clear. It has been rephrased.

Fig. 5: add x-axis label, Time (UTC) or similar.
Done.

Page 14 Line 1: What do you mean by "water current" exactly? Do you mean depth-mean?
No, it is the surface current. It has been changed.

Page 14 Line 1: what do you mean by "mean differences"? I think you mean the "mean of the hourly instantaneous difference". I would rephrase.
Right, it has been rephrased.

Fig. 9: I suggest you use the same x-axis range as Fig. 5, or would this make it harder to make your point in the text?
Yes, it is reasonable to use the same x-axis range. It has been fixed.

Page 22 Line 25: . . . results have demonstrated to be physically reasonable, being capable of reproducing the well . . . –> . . . results are physically reasonable, as they reproduce the well . . .
Fixed.

Page 22 Line 25: This has allowed to investigate the impact of the WCIs . . . –> The results have enabled the WCIs to be investigated . . .
Fixed.

Anonymous Referee #2

The authors acknowledge the helpful comments and corrections of Referee #2, which helped to improve the quality of the manuscript. Below, each comment is answered point-by-point. A marked-up version of the manuscript with the corrections is enclosed as a supplement file. This version also include the corrections due to the comments by Referee #1.

This work presents some results provided by a ocean/wave high resolution coupled model, comparing with uncoupled runs and observations.

I would suggests to clarify the conclusions in the abstract. For example, it is said that ’the agreement of the modeled wave period improves...’, but not respect to what.
The results explanation in the abstract has been improved.

I would like to see in the introduction how previous research work relates to the current research. For example, given that this work uses a high resolution model (350m), if the coupling influence depends on resolution in some way.
A new paragraph has been added at the introduction section in order to relate with previous work about WCIs. A comment on the grid resolution dependency has also been included.

Very often the authors comment on ’the current effect on waves’, and care should be taken here as they are also coupling the sea surface height and the effect of both will have an influence in the results. Furthermore, in a two-way coupled model there will be a feedback between one model and the other, so that what they will observe will be the overall effect of coupling one model to the other.
Right, with "the current effect on waves" we wanted to say the effect on the wave field when the models were coupled, i.e. when the wave model included the effects of being coupled with the circulation model but not only and strictly the "current effects". This expression has been changed by "coupling effects on waves" all along the manuscript. Besides, in order to follow the same criteria, the expression "wave effects on currents" has been changed to "coupling effects on currents".

The text should clarify if the instantaneous values of the coupling fields are passed between models at every coupling time step (20 minutes), or the average value between coupling steps.
The coupling uses instantaneous fields. The explanation in the manuscript has been improved (page 7 lines 14-15).

Table 1 should clarify if the winds are the 10m winds or the winds interpolated to 3m.
In order to be able to compare the modeled winds with the measured ones, the winds in Table 1 are at 3m. It has been specified in the table caption and in the manuscript text.

In the text or the table caption it is not well described the meaning of ’uncS’ or ’cRS’.
Due to the previous revision of Referee #1, the naming of the different runs were included in the manuscript text in the first paragraph of section 2.3.2.

In the text some expressions such as Tm02 are used before their meaning is explained.
Right, the Tm02 was used before it was defined. This has been corrected in the new version of the manuscript.

The surface stresses are calculated by the changes in surface roughness. The expression for the surface roughness here is different to the one used to interpolate 10m to 3m winds, and it should be clarified why the same expression is not used in both cases. In the second case, there is the possibility of using the actual Charnock parameter that can be provided by the wave model, instead of using a default value.

As we understand it, two methods have to be distinguished. On the one hand, there is the formula used to extrapolate the wind data in order to be able to compare them with the measurements. This is used to calculate the statistical parameters (i.e., analyze the wind data quality) and to find the wind-jet events. On the other hand, there are the formulas used by the numerical model to compute the surface roughness, which are different in the uncR run and the cRS run (in the second case it will depend on the wave parameters but in the first case it will not). Maybe this could lead to some confusion, but we think it is important not to merge these different methodologies.

It should be better justified why it is considered that 24 hours are enough to spin-up the model.

The decision of using 24 h is based on different things: our knowledge of our models behavior, the analysis of the time series and the model configurations. We have to keep in mind that the ROMS model is initialized with data from IBI-MFC, so the spin-up time is expected to be short. A brief explanation has been added in the manuscript (page 9 lines 15-17).

One important conclusion is that the largest differences between coupled and uncoupled runs take place at shallower areas, but this is illustrated just by comparing results in two points in the domain. What I miss is a whole domain picture showing differences in some variable between coupled and uncoupled results to actually confirm that the largest differences occur at shallow places, instead of resulting of a fortunate selection of comparison sites.

According to our interpretation of this point, the current and Hs differences between coupled and uncoupled runs in the whole domain are already shown in Figure 7. This figure shows how the larger effects take place at shallow regions.

The article is centered in wave effects on currents, but might be it would be useful to look at other variables such as sea temperature or salinity, as they might better illustrate the effect of vertical mixing.

The effect of vertical mixing is shown by means of the Brunt-Väisälä frequency, which includes the temperature and salinity information. We have figures with the temperature and salinity evolution during the wind-jet event (see below) but we believe that they do not provide new information and it would be redundant. For this reason, we believe that it is better to not show these figures. It would increase the number of figures in the manuscript without giving additional information.

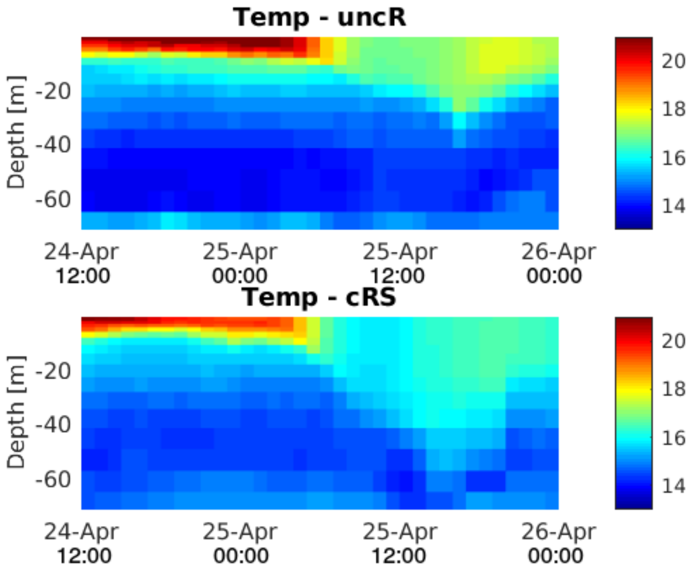

Figure 1. Temperature evolution throughout the wind-jet event E3 at point P1.

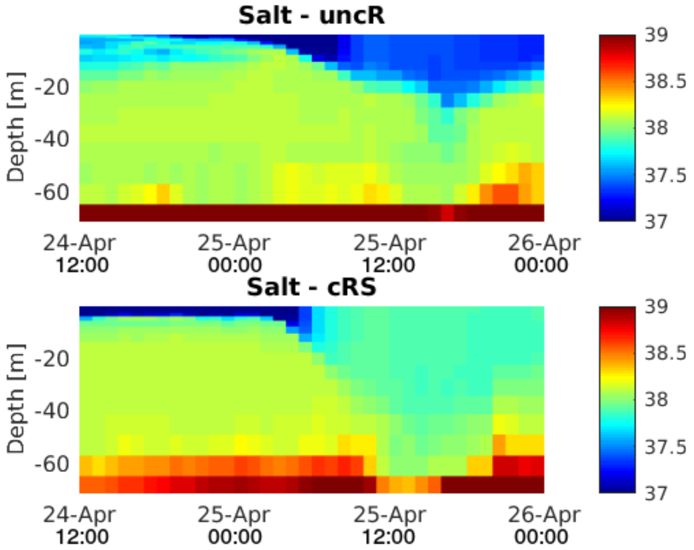

Figure 2. Salinity evolution throughout the wind-jet event E3 at point P1.

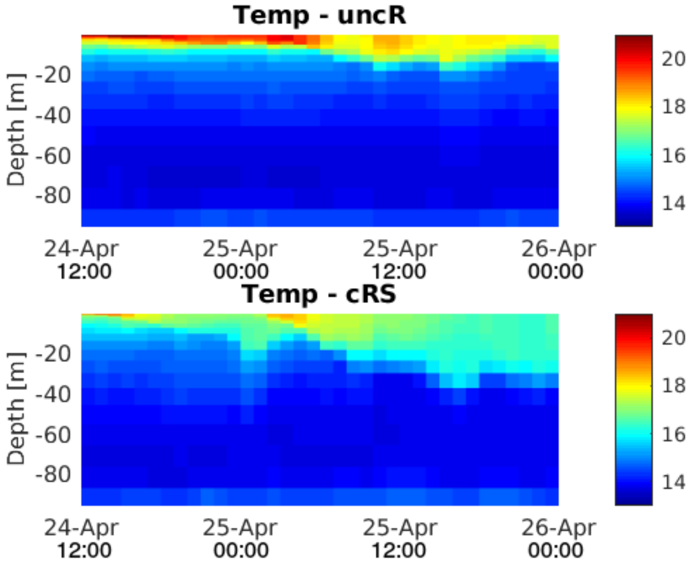

Figure 3. Temperature evolution throughout the wind-jet event E3 at point P3.

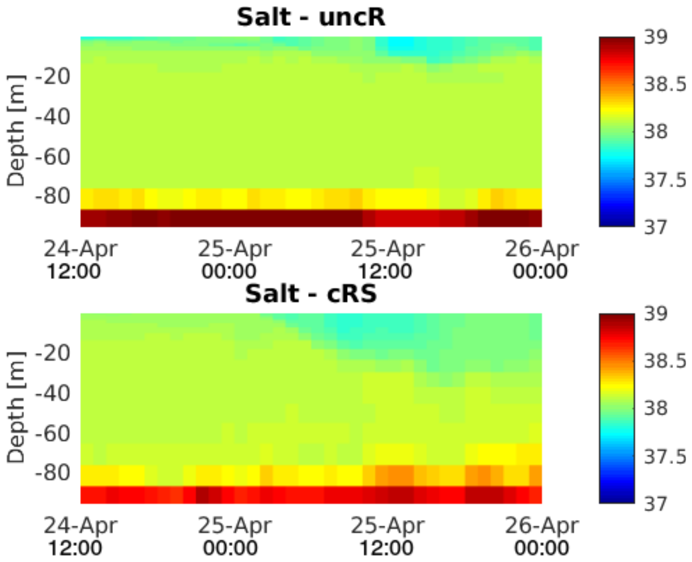

Figure 4. Salinity evolution throughout the wind-jet event E3 at point P3.

Wave–Current Interactions in a Wind-jet Region

Laura Ràfols[a,b], Manel Grifoll[a], and Manuel Espino[a]

[a]Maritime Engineering Laboratory (LIM-UPC), Polytechnic University of Catalonia (BarcelonaTech), C/ Jordi Girona 1-3 Edif. D1, 08034 Barcelona, Spain
[b]Meteorological Service of Catalonia (SMC), C/ Berlin 38-48 4a, 08029 Barcelona, Spain

Correspondence: Laura Ràfols (laura.rafols@upc.edu)

Abstract. Wave–Current Interactions (WCIs) are investigated. The study area is located at the northern margin of the Ebro Shelf (northwestern Mediterranean Sea), where episodes of strong cross-shelf wind (wind jets) occur. The aim of this study is to validate the implemented coupled system and investigate the impact of WCIs on the hydrodynamics of a wind-jet region. The Coupled Ocean–Atmosphere–Wave–Sediment Transport (COAWST) modeling system, which use Regional Ocean Model System (ROMS) and Simulating WAves Nearshore (SWAN) models, is used in a high-resolution domain (350 m). Results from uncoupled numerical models are compared with a two-way coupling simulation. The results do not show substantial differences in the water current field between the coupled and the uncoupled runs. The main effect observed when the ~~waves are considered~~ models are coupled is in the water column stratification, due to the turbulent kinetic energy injection and the enhanced surface stress, leading to a larger mixed-layer depth. ~~Additionally, when the water currents are considered~~Regarding the effects on the wave fields, the comparison between the coupled and the uncoupled runs show that, when the models are coupled, the agreement of the modeled wave period significantly improves and the wave energy (and thus the significant wave height) decreases when the current flows in the same direction as the waves propagate.

1 Introduction

During the last decade, several water circulation models have been developed including the wind-waves induced currents. There are two different formulations to include the so-called wave effects on currents (WEC) in the three-dimensional primitive equations: by means of the radiation stress gradient (Mellor, 2011) and with the vortex force (VF) formalism (Uchiyama et al., 2010; Kumar et al., 2012). The VF formalism separates the conservative and non-conservative contributions in the momentum balance equations, which allows one to evaluate flow fields within both inner shelf and surf zone environments (Kumar et al., 2012).

From a modeling perspective, several circulation and wave models have been coupled in order to consider the wave–current interactions (WCIs). For instance, Xie et al. (2001) coupled the 3D ocean model POM with the WAM wave model and found that wind waves can significantly affect coastal ocean currents both at the surface and near the seabed. Osuna and Wolf (2005) implemented the coupling between the circulation Proudman Oceanographic Laboratory Coastal-Ocean Modeling System (POLCOMS) and the WAM model in the Irish Sea. This system was then modified by Bolaños et al. (2011), who included three-dimensional interactions following Mellor (2003, 2005) and applied the coupled model system to the Mediterranean Sea. Tang et al. (2007) implemented the WCI in a 3D ocean model (Princeton Ocean Model, POM) and a spectral wave model (WAVEWATCH III), based on Jenkins (1987) formulation, and evaluated the model by comparison with surface velocity data derived from surface drifters. McWilliams et al. (2004) developed a multi-scale asymptotic theory for the evolution and interaction of currents and surface gravity waves of finite depth, which was then implemented and extended for applications within the surf zone in the UCLA ROMS model by Uchiyama et al. (2010). Warner et al. (2008b) used the Model Coupling Toolkit (MCT) to couple the ocean circulation model Regional Ocean Model System (ROMS) and the surface wave model Simulating WAves Nearshore (SWAN) and included nearshore processes, such as radiation-stress terms based on Mellor (2003, 2005) and a surface roller model (Svendsen, 1984; Svendsen et al., 2002). This system was then further developed by Warner et al. (2010) to include one-way grid refinement in the oceanic and wave models, coupling to an atmospheric model in order to include effects of sea surface temperature and waves, and to provide interpolation mechanisms to allow the models to compute on different grids. The resulting system is known as the Coupled Ocean–Atmosphere–Wave–Sediment Transport (COAWST) modeling system. Then, Kumar et al. (2012) implemented the VF formalism into the COAWST modeling system, with some modifications to the method of Uchiyama et al. (2010).

Previous studies have analyzed the physical processes involved in the WCIs and the relevance of the coupling effects can vary depending, mainly, on the water depth and the energy of the studied event. The WCIs have demonstrated to be important at coastal regions (Wolf and Prandle, 1999; Kumar et al., 2012; Liang et al., 2017), estuaries (Olabarrieta et al., 2011; Bolaños et al., 2014) and during energetic events such as hurricanes or strong wind events (Xie et al., 2008; Sheng et al., 2010; Renault et al., 2012; Benetazzo et

. As a matter of fact, the previous cited studies have different focuses and are applied to different domain types (going from seas to surf zones and estuaries) and thus the grid resolutions used in these studies varies from few meters to few kilometers. For instance, Osuna and Wolf (2005) studied the coupling effects in the Irish Sea, Benetazzo et al. (2013) analyzed the WCI in a semi-enclosed basin with particular focus on events associated to prevailing and dominant winds of the region and Kumar et al. (2012) applied different WCI tests at coastal regions, including the study of obliquely incident waves on a planar beach and the analysis of the wave-induced cross shore flows in the inner shelf.

The north Ebro Shelf (NW Mediterranean Sea) is a region characterized by northwestern (NW) winds that are channeled through the Ebro Valley and which result in cross-shelf wind jets when they reach the sea. This region is very interesting from a meteo-oceanographic point of view because multiple processes take place, such as bimodal wave spectra and the development of a two-layer cross-shelf flow. Some authors have investigated the circulation patterns (Grifoll et al., 2015; Ràfols et al., 2017a) and the wave field (Bolaños-Sanchez et al., 2007; Grifoll et al., 2016; Ràfols et al., 2017b) during these NW wind-jet events but less efforts have been made at investigating the WCI in the region. Due to the limited observational data, in order to study the wind-jet induced dynamics of the region, the use of numerical models is required. However, at the same time, this makes the investigation rather challenging and forces a rather qualitative analysis based on the modeled physical processes reliability. The purpose of this study is to validate the implemented coupled system and investigate the ~~wave~~ coupling effects on the circulation and the ~~current effects on the~~ wave field at the continental shelf during a wind-jet event. With this aim, results from uncoupled models are compared with the outputs from a two-way coupled numerical model. The selected study period is from March 15 2014 to May 15 2014 because it contains four wind-jet episodes. Additionally, this period has ~~been previously~~ previously been used to validate numerical models in the study region, and the wind-wave characterization (Ràfols et al., 2017b) ~~,~~ and water shelf circulation (Ràfols et al., 2017a) ~~was~~ were investigated by combining numerical efforts and in situ observations.

This work is organized as follows. In Section 2 the study area and the methods used in this work are presented. The results are shown in Section 3, discerning between the ~~effects of waves~~ coupling effects on currents and the ~~effects of currents~~ coupling effects on waves. A discussion of the results can be found in Section 4, and the main conclusions of the work are highlighted in Section 5.

2 Study area and methodology

2.1 Study area

The north Ebro Shelf is located at the southern part of the Catalan coast, at 40.4°–41.1° N and 0.4°–1.3° E (see Fig. 1). The shelf of this region is characterized by the transition from a narrow shelf (∼10km) at its northern margin to a broader shelf (∼60 km) towards the south.

The most characteristic wind of the region is the northwesterly wind (mistral), which is channeled through the Ebro Valley resulting in a cross-shelf wind jet when it reaches the sea. This wind jet is related to the presence of a high-pressure area over the Iberian Peninsula and a low-pressure area over the Mediterranean Sea. Thus, it is more common during autumn and winter (Grifoll et al., 2015), when large atmospheric pressure gradients occur. The predominant regional current is the quasi-permanent slope current known as the Northern Current, which is an entity flowing along the continental slope (Millot, 1999) that can be modified by mesoscale events such as current meandering or eddies (Font et al., 1995). The water circulation in the inner and mid-shelf presents strong temporal and spatial variability due to the strong gradients in the bathymetry and wind field associated with wind-jet episodes (Grifoll et al., 2015; Ràfols et al., 2017a). The wave climate at the Ebro Delta is characterized by the predominance of NW winds (which coincides with the predominance of NW winds), although there are also significant storms from the east and south. These storms tend to develop a bimodal directional spectrum due to the coexistence of wind waves and swell waves (Sánchez-Arcilla et al., 2008; Ràfols et al., 2017b). Local wind waves (sea system) show a broadband spectrum with a high variety of frequencies associated with irregular sea states. In contrast, waves generated far away (swell system) present a narrowband spectrum with a frequency range with less associated energy. Then, when the sea and swell systems exist at the same time, bimodal spectra occur (Ràfols et al., 2017b).

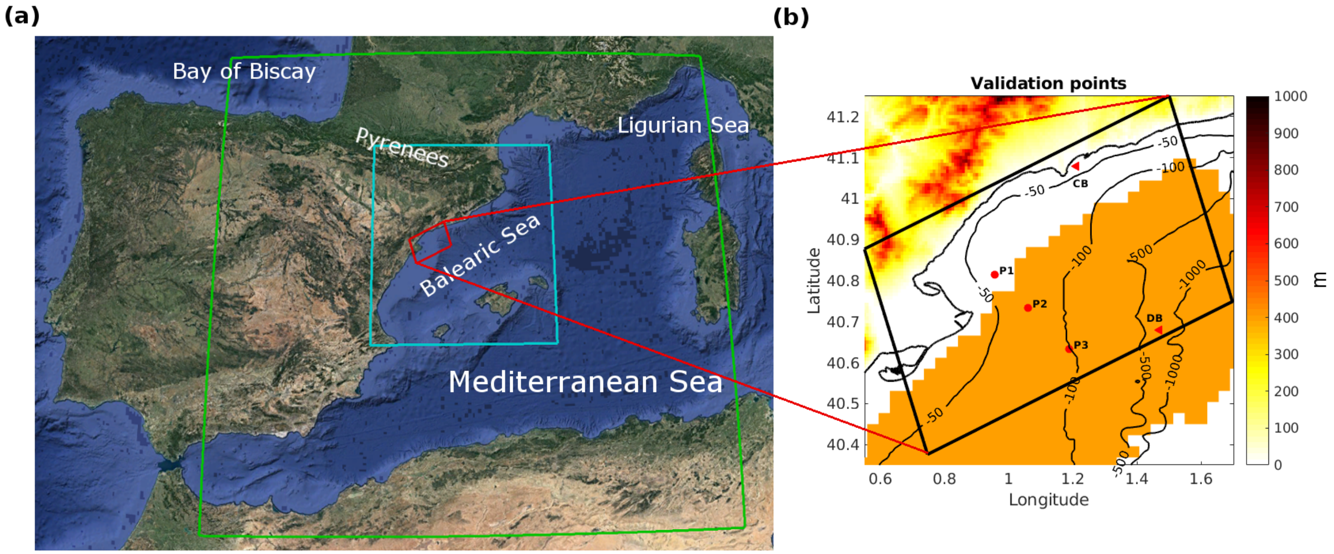

Figure 1. Study area. (a) NW Mediterranean Sea and numerical domains: 15 km resolution domain for the SWAN model (green), 3 km resolution domain for the SWAN model (blue) and 350 m resolution coastal domain for the ROMS and SWAN models (red). (b) Orography (in m), coastal domain, buoy locations (red triangles; CB and DB), points where the numerical results are examined in detail (red dots: P1, P2 and P3) and HF radar coverage area (in orange).

2.2 Data

For validation purposes, oceanographic and coastal meteorological measurements from Puertos del Estado (http://www.puertos.es) are used. Specifically, data were obtained from a coastal wave buoy, a deep-water buoy and ~~an~~ high-frequency (HF) radar. The locations are shown in Fig. 1, jointly with the bathymetry and the numerical domains.

The coastal wave buoy (CB) is a Triaxys buoy located at 41.07° N, 1.19° E at 15 m depth, deployed in November 1992. It provides significant wave height, peak period, nautical direction and directional wave spectra, among other data. The deep-water buoy (DB), an ocean Seawatch buoy located at 40.68° N, 1.47° E at 688 m depth was deployed in August 2004. This buoy measures water velocity and water temperature at the sub-surface (nominal depth of 3 m), wind vectors at 3 m above the sea surface, significant wave height, peak period, nautical direction and directional wave spectra, among other parameters. In order to be able to compare the measured wind data at 3 m height with the modeled data at 10 m height, the modeled data have been extrapolated from 10 m to 3 m using a logarithmic profile (see Appendix A).

The HF radar system used in this work is a CODAR SeaSonde standard-range system composed of three remote shelf-based sites that became operational in December 2013. Each site comprises a transmitter–receiver antenna that operates at a nominal frequency of 13.5 MHz with a 90 ~~KHz~~ kHz bandwidth. The system provides hourly measurements of the current velocities in the top meter of the water column with a horizontal resolution of 3 km and a cut-off filter of 100 cm/s. More information about the system is available in Lorente et al. (2015).

2.3 Numerical models

2.3.1 COAWST modeling system description

The COAWST Modeling System (Warner et al., 2010) has been widely used by many authors to investigate the WCI (Olabarrieta et al., 2011; Renault et al., 2012; Benetazzo et al., 2013; Rong et al., 2014; Grifoll et al., 2014; Bruneau and Toumi, 2016, among others). In this study, the COAWST modeling system is used to perform the uncoupled ROMS and SWAN model simulations and ~~the two-ways coupling run~~ a model run with two-way coupling.

The SWAN model is a third-generation numerical wave model that computes random, short-crested waves in coastal regions with shallow water and ambient currents (Booij et al., 1999). It is based on the action balance equation in terms of action density ~~N~~ (Bretherton and Garrett, 1968) with sources and sinks and incorporates state-of-the-art formulations of wave–wave interactions and the processes of wave generation and dissipation.

The ROMS model is a split-explicit, free-surface, terrain-following, primitive equations oceanic model that solves the 3D Reynolds-Averaged Navier–Stokes equations using the hydrostatic and Boussinesq assumptions (Shchepetkin and McWilliams, 2005; Haidvogel et al., 2008). The model uses finite-difference approximations on a terrain-following vertical coordinate (sigma coordinate) and on a horizontal curvilinear Arakawa C grid.

The Model Coupling Toolkit (MCT; Larson et al., 2004; Jacob et al., 2004) is a Fortran90 program that works with the MPI protocol. It allows the transmission and transformation of various distributed data between component models using a parallel coupled approach. When the models are initialized, each model decomposes its own domain into different sections, which are distributed to processors. On each processor, each grid section initializes into MCT and a global map of the distribution of the segments is computed. Each segment also initializes an attribute vector that contains the fields to be exchanged and establishes a router to provide an exchange pathway between model components. While the simulation is run, the models reach a synchronization point, fill the attribute vectors with data and exchange fields. Further details are described in Warner et al. (2008a).

2.3.2 System set-up

Three different runs have been performed in this work (see Fig. 2): one with the ROMS model uncoupled (*uncR*), one with the SWAN model uncoupled (*uncS*) and, finally, one with the ROMS and SWAN models two-way coupled (*cRS*).

The numerical domain has a horizontal resolution of 350 m and, in the ROMS case, a vertical resolution of 20 sigma levels. The bathymetry introduced in the models has a grid resolution of 0.0083° and was obtained from General Bathymetric Chart of the Oceans (GEBCO; www.gebco.net). Both SWAN and ROMS models are forced with hourly atmospheric data from a previous WRF (Weather Research and Forecasting) model run provided by the SMC (Servei Meteorològic de Catalunya) that has a spatial resolution of 3 km.

In order to generate the boundary conditions for the SWAN model, a downscaling technique has been used. The entire system consists of three nested domains (see Fig. 1a). The largest one covers the western Mediterranean Sea with a spatial resolution of 15 km and provides boundary conditions to a second-level domain. The latter covers the Balearic Sea with a

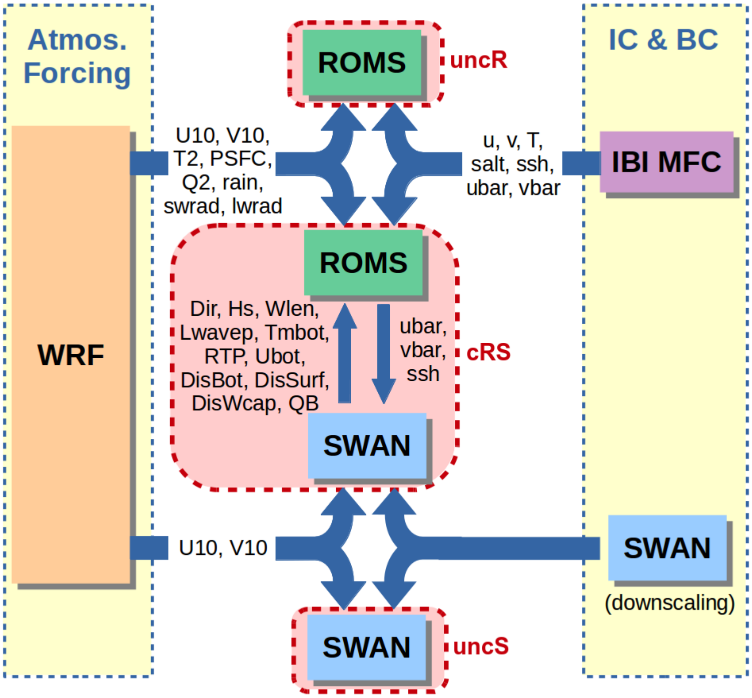

Figure 2. Configuration of setup run. In red, the name given to each configuration.

spatial resolution of 3 km and provides boundary conditions to the smaller domain, which has a horizontal resolution of 350 m. This study is focused on this last domain. The nesting between each domain consist on providing the energy spectra from the coarser domain to the boundary of the smaller domain. The WRF model provided by the SMC provides the 10-m surface winds ($U10$, $V10$) forcing and the initial conditions have been obtained running the model in stationary mode.

In the SWAN model, non-stationary conditions, spherical coordinates and nautical convention have been selected. The wave growth by wind is computed with a sum of a linear term and an exponential term. For the linear growth, the expression from Cavaleri and Malanotte-Rizzoli (1981) is used, and for the exponential growth, the expression and coefficients from Komen et al. (1984) are used. The nonlinear quadruplet wave interactions are integrated by a fully explicit computation of the nonlinear transfer with the Discrete Interaction Approximation (DIA; proposed by Hasselmann et al., 1985) per sweep (using default coefficients). For the whitecapping, the Komen et al. (1984) formulation is used with $C_{ds} = 2.36 \times 10^{-5}$, $\delta = 1$ and $p = 4$. Finally, the JONSWAP (Hasselmann et al., 1973) bottom friction formulation is added with the default coefficients. The spectrum is discretized with a constant relative frequency resolution of $\Delta f = 1.1$ (logarithmic distribution) and a constant directional resolution of $\Delta\theta = 10°$. The discrete frequencies are defined between 0.01 Hz and 1 Hz. Above the high-frequency cutoff, a diagnostic tail f^{-4} is added.

The initial and boundary conditions for the ROMS model are taken from the Iberian Biscay Irish – Monitoring and Forecasting Centre (IBI-MFC) product. This product (http://marine.copernicus.eu/) includes all main forcings (i.e. tidal forcing, high-frequency atmospheric forcing, fresh water river discharge, etc.) and is based on a (eddy-resolving) NEMO model application run at 1/36° horizontal resolution. The outputs provided by the IBI-MFC used in our numerical model are 3D daily means of temperature (T), salinity ($salt$) zonal velocity (u), meridional velocity (v) and 2D (surface) hourly means of sea surface height (ssh) and barotropic currents ($ubar$, $vbar$). The WRF model provided by the SMC provides the atmospheric forcing fields for the ROMS model, which include 10 m surface winds ($U10$, $V10$), atmospheric pressure ($PSFC$), relative humidity ($Q2$), atmospheric surface temperature ($T2$), precipitation ($rain$) and shortwave ($swrad$) and longwave ($lwrad$) net heat fluxes to the ocean model. The model uses these parameters in the COARE algorithm (Fairall et al., 1996) to compute ocean surface stresses and ocean surface net heat fluxes.

The ROMS model implementation includes a generic length-scale turbulent vertical mixing scheme with the $k-\epsilon$ parametrization, a logarithmic profile for the bottom boundary layer with a bottom roughness of 0.005 m and horizontal mixing terms in geopotential surfaces. The Ebro River discharge is characterized with data from the Automatic Hydrologic Information System of the Ebro River basin (owned by the Confederación Hidrográfica del Ebro, www.chebro.es). The data used to force the numerical model consist of daily measurements of river runoff and temperature.

In the two-way coupled run, the ~~WEC are implemented using a coupling time step of~~ WCIs are implemented exchanging instantaneous values of coupling fields every 20 min. The wave model provides wave direction (Dir), significant wave height (Hs), wave length ($Wlen$), peak wave length ($Lwavep$), surface and bottom periods (RTP, $Tmbot$), bottom orbital velocity ($Ubot$), wave energy dissipation ($DisBot$, $DisSurf$, $DisWcap$) and percent wave breaking (QB) to the ocean model. These parameters are used by the ocean model in four different mechanisms:

- To compute enhanced bottom stresses due to the effect of turbulence in the wave boundary layer by means of the SSW (Sherwood / Signell / Warner) implementation of Madsen (1994) bottom boundary layer formulation.
- To compute enhanced surface stresses (SStr) due to changes in the surface roughness z_0. In contrast to the COARE algorithm used in the uncoupled ROMS run, now the Taylor and Yelland (2001) sea surface roughness closure model, which is sea-state dependent, is used. Now the z_0 is derived from $\frac{z_0}{Hs} = 1200(Hs/Lp)^{4.5}$, where Lp is the peak wave length.
- To inject turbulent kinetic energy (TKE) at the surface due to breaking waves. It is introduced as a surface flux of turbulence kinetic energy in the generic length scale method (Warner et al., 2005).
- To include the wave forces using the VF formalism (Uchiyama et al., 2010; Kumar et al., 2012, ; see Section 2.4).

The wave model receives currents (u_s, v_s) and sea surface height (ssh) from the ocean model. The surface currents (u_s, v_s) were computed taking into account the vertical distribution of the current profile using the formulation presented by Kirby and Chen (1989), which integrates the near-surface velocity over a depth controlled by the wave number. The presence of an ambient current may change the amplitude (e.g. due to an energy transfer between waves and currents), the frequency (due to the Doppler shift) and the direction (due to current-induced refraction) of the waves. In this sense, the ocean currents modify the wind speed forcing with $S = f(U_{wind} - u_s; V_{wind} - v_s)$, the wave celerity using the modified group velocities $c_x = c_{gx} + u_s$, $c_y = c_{gy} + v_s$ and the wave number (derived from the Doppler shift effect; see Holthuijsen (2008), Appendix D).

2.4 Momentum balance description

The cross-shelf momentum balance is used to analyze the ~~wave~~ coupling effects on the circulation over the continental shelf. The simplified equations for the VF approach can be obtained after removing the curvilinear terms, body forces and horizontal and vertical mixing, and then using Cartesian coordinates (Kumar, 2013):

$$\frac{\partial \overline{v}}{\partial t} + \frac{1}{H}\left[\frac{\partial}{\partial x}\left(\int uvdz\right) + \overline{v}\left(\frac{\partial}{\partial x}\int u^{st}dz\right) + \overline{v}\left(\frac{\partial}{\partial y}\int v^{st}dz\right)\right] + \tag{1}$$

$$\frac{\overline{u^{st}}}{H}\left[\frac{\partial}{\partial x}\left(\int vdz\right) - \frac{\partial}{\partial y}\left(\int udz\right)\right] + f\overline{u} + f\overline{u^{st}} = -\frac{1}{\rho_0}\frac{\partial p}{\partial y} + \overline{F^{wy}} + \frac{\tau_s^y}{\rho_0 H} - \frac{\tau_b^y}{\rho_0 H}$$

where u and v are the along-shore and cross shore velocity components, u^{st} and v^{st} are the Stokes velocities, the overbar indicates depth averaging, H is the total water depth, f is the Coriolis parameter, ρ_0 is the reference density, τ_s^y and τ_b^y are the surface and bottom stress, respectively, and F^{wy} is the non-conservative wave forcing. Going from left to right, the terms in the equations are local acceleration (*ACC*), horizontal advection (*HA*), horizontal vortex force (*HVF*), Coriolis (*COR*), Stokes–Coriolis (*StCOR*), pressure gradient (*PG*), non-conservative wave forces (*WF*), surface stress (*SStr*) and bottom stress (*BStr*). Terms in blue are the wave-induced terms.

The pressure gradient term includes (Kumar et al., 2012) the Eulerian non-WEC contribution (P^c) and the WEC contribution (P^{WEC}), which can be decomposed in a quasi-static response (P^{qs}), a Bernoulli head (P^{bh}) and a surface pressure boundary correction (P^{pc}):

$$\nabla\varphi = P^c + P^{WEC} = P^c + P^{qs} + P^{bh} + P^{pc} \tag{2}$$

The non-conservative wave forcing term F^{wy} includes accelerations due to (Kumar et al., 2012): bottom streaming (B^{bf}), surface streaming (B^{sf}) and wave breaking (B^{wb}). The latter is further decomposed in whitecapping induced acceleration (B^{wcap}), bathymetry induced breaking and acceleration (B^b) and wave rollers and rollers acceleration (B^r):

$$F^{wy} = B^{bf} + B^{sf} + B^{wb} = B^{bf} + B^{sf} + B^{wcap} + B^b + B^r \tag{3}$$

2.5 Skill assessment techniques

In order to assess the model behavior, the estimation of bias, the root mean square deviation (RMSD), the Pearson's correlation (Pearson's r) and the model skill score (d, following the method presented in Willmott (1981)) are undertaken. These values are defined as follows:

$$bias = \frac{1}{N}\sum\left(X_{model} - X_{obs}\right) \tag{4}$$

$$RMSD = \sqrt{\frac{1}{N}\sum\left(X_{model} - X_{obs}\right)^2} \tag{5}$$

$$r = \frac{\sum\left(\left(X_{model} - \overline{X_{model}}\right)\left(X_{obs} - \overline{X_{obs}}\right)\right)}{\sqrt{\sum\left(X_{model} - \overline{X_{model}}\right)^2}\sqrt{\sum\left(X_{obs} - \overline{X_{obs}}\right)^2}} \tag{6}$$

$$d = 1 - \frac{\sum\left|X_{model} - X_{obs}\right|^2}{\sum\left(\left|X_{model} - \overline{X_{obs}}\right| + \left|X_{obs} - \overline{X_{obs}}\right|\right)^2} \tag{7}$$

where N is the number of samples. Pearson's r describes consistent proportional increases or decreases about respective means of the two quantities, but it makes too few distinctions among the type or magnitudes of possible covariations (Willmott, 1981). By contrast, d is not a measure of correlation or association in the formal sense but rather a measure of the degree to which a model's predictions are error-free. Unlike r, d is sensitive to differences between the observed and predicted means as well as to certain changes in proportionality (Willmott, 1981). Note that analogously to r, d is measured from 0 to 1, 1 denoting maximum agreement. When computing these metrics, the first 24 h of the model results were rejected, in order to exclude the possible spin-up of the model. The time series analyses have demonstrated that 24 h are enougth to spin-up the model. Besides it has to be noticed that the ROMS model is not initialized from zero velocities, it reads the initial conditions from the IBI-MFC model.

For circular data, e.g. wave direction, the metrics are computed as follows:

$$bias = \tan^{-1}\left(\frac{\frac{1}{N}\sum\sin\left(X_{model} - X_{obs}\right)}{\frac{1}{N}\sum\cos\left(X_{model} - X_{obs}\right)}\right) \tag{8}$$

$$RMSD = \sqrt{-2\cdot\ln\left(\frac{1}{N}\sum\cos\left(X_{obs} - X_{model}\right)\right)} \tag{9}$$

$$r = \frac{\sum\left(\sin\left(X_{model} - \overline{X_{model}}\right)\sin\left(X_{obs} - \overline{X_{obs}}\right)\right)}{\sqrt{\sum\sin^2\left(X_{model} - \overline{X_{model}}\right)\sum\sin^2\left(X_{obs} - \overline{X_{obs}}\right)}} \tag{10}$$

3 Results

3.1 Numerical model skill assessment

The ROMS and SWAN models for the same study period and the same model configurations have been validated thoroughly in previous studies (Ràfols et al., 2017a, b). The aim of this section is to analyze the skill of the coupled run in comparison to the uncoupled runs.

The first step in the numerical skill assessment is to examine the quality of the wind field, which is used to force the numerical models. Table 1 shows the bias, RMSD, r and d obtained from the comparison between the DB measured data and the wind field provided by the SMC ~~. And Fig.~~(which has been extrapolated from 10 m to 3 m). Figure 3 presents the time series for the modeled and measured wind intensity at DB. The comparison shows a slight underestimation of the wind intensity but the main underestimation does not correspond to the NW wind events, which are the focus of this study. During the study period, four NW wind-jet events have been selected (see the red boxes in Fig. 3). These events were previously analyzed in Ràfols et al. (2017b), where statistical metrics for each episode were provided. To see the temporal evolution of a wind jet more clearly, in Fig. 4a the time series during the wind-jet event E3 are presented, which is the event that spans more in space and thus can be observed in the DB location. Overall, the modeled wind during the wind-jet events is less underestimated and the wind-jet temporal evolutions are properly reproduced.

Table 1. Statistics comparing the 3m wind and the modeled wave parameters with the DB data.

		bias	RMSD	r	d
Wind		-0.04 m/s	1.83 m/s	0.83	0.89
Hs	*uncS*	-0.25 m	0.38 m	0.89	0.86
	cRS	-0.28 m	0.40 m	0.90	0.85
Tm_{02}	*uncS*	-0.95 s	1.09 s	0.79	0.67
	cRS	-0.34 s	0.52 s	0.85	0.86
Dir	*uncS*	-9.39°	34.89°	0.84	–
	cRS	-10.34°	36.37°	0.84	–

Table 1 also shows the statistics obtained from the comparison of the measured wave parameters at DB and the modeled ones. The Hs and Tm_{02} time series at DB during the wind-jet event E3 are shown in Fig. 4b and Fig. 4c, respectively. ~~In general, the Hs does not show relevant differences between the *uncS* run and the *cRS* run results. It is important to note the negative bias, which indicates that the Hs parameter is slightly underestimated. This is a clear consequence of the previously~~

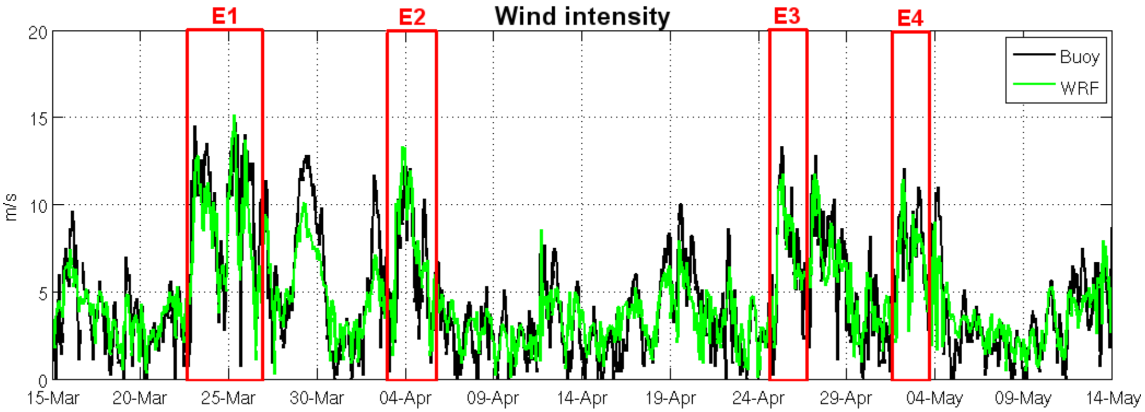

Figure 3. Comparison between the wind measured by the DB buoy (black) and the one modeled by the WRF model and used as input for the SWAN and ROMS models (green). See statistics in Table 1. The red boxes are the four wind-jet events.

~~mentioned underestimation of the wind. In contrast, Tm_{02} shows a clear improvement when the models are coupled.~~ The mean wave period Tm_{02} is defined as follows:

$$Tm_{02} = 2\pi \left(\frac{\int\int \omega^2 E(\omega,\theta) d\omega d\theta}{\int\int E(\omega,\theta) d\omega d\theta} \right)^{-1/2} \tag{11}$$

where $E(\omega,\theta)$ is the variance density and ω is the absolute radian frequency. The latter is determined by the Doppler shift phenomenon with $\omega = \sigma + \mathbf{k}\cdot\mathbf{U}$, where σ is the relative radian frequency (i.e. as observed in a frame of reference moving with the current velocity), $\mathbf{k}$ the wave number vector and $\mathbf{U}$ the current vector. In absence of currents, the relative radian frequency equals the absolute radian frequency. Regarding the Table 1 results, in general, the Hs does not show relevant differences between the *uncS* run and the *cRS* run results. It is important to note ~~that the~~ the negative bias, which indicates that the Hs parameter is slightly underestimated. This is a clear consequence of the previously mentioned underestimation of the wind. In contrast, Tm_{02} shows a clear improvement when the models are coupled. In this case, keeping in mind the Tm_{02} definition, it is important to note that the buoy measures at a fixed location (i.e. in an absolute frame) and, for this reason, the comparison of the measured period with the modeled one is more realistic when the results from the *cRS* run are used (i.e. the absolute period) instead of the results from the *uncR* run (i.e. the relative period). Therefore, the differences found in the Tm_{02} parameter might be explained, in part but not uniquely, by the differences in frequency due to the Doppler shift phenomena that are included in the wave model when the models are coupled.

Table 2, where the modeled data are compared with measurements from CB, show similar results to Table 1. The most noticeable difference between the two tables is the Dir parameter, which shows better agreement in the DB case. The comparison at DB shows very good results with strong correlations and no relevant differences between the *uncS* and *cRS* runs. In contrast, at CB location, the agreement with observations is smaller but a clear improvement of the results is obtained when the currents are considered (i.e. with the *cRS* run).

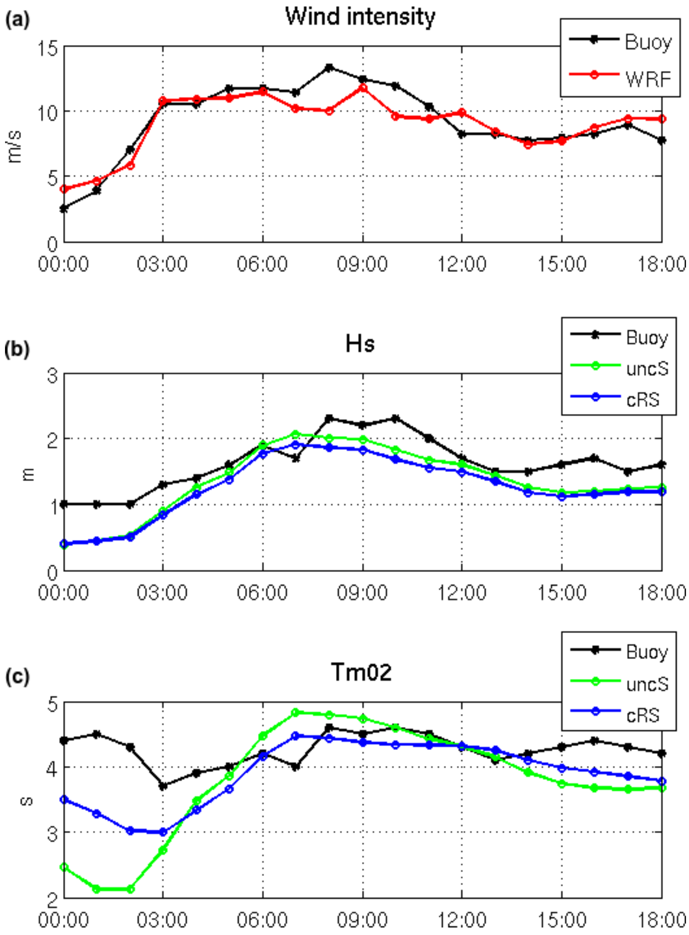

Figure 4. (a) Wind intensity, (b) Hs and (c) Tm_{02} time series at DB during the wind-jet event E3 (25 April 2014). In black, the measured data, in red the WRF model data, in green the *uncS* run results and in blue the *cRS* run results.

Table 2. Statistics comparing the modeled wave parameters with the CB data.

		bias	RMSD	r	d
Hs	*uncS*	-0.14 m	0.23 m	0.87	0.79
	cRS	-0.17 m	0.24 m	0.89	0.79
Tm_{02}	*uncS*	-1.24 s	1.43 s	0.42	0.48
	cRS	-0.34 s	0.64 s	0.71	0.79
Dir	*uncS*	4.11°	33.06°	0.46	–
	cRS	-0.99°	25.97°	0.52	–

In Table 3, the modeled water currents are compared with the HF radar surface current measurements. The metrics presented in the table correspond to point P3 and show good agreement, with skill metrics that are in accordance with values found in previous work when comparing HF radar data with modeled data (Port et al., 2011; O'Donncha et al., 2015; Lorente et al., 2016). Comparing the results from the *uncR* run with the results from the *cRS* run, some differences are observed (e.g. a decrease of the bias is obtained in the cross-shelf velocity component when the models are coupled), but the differences are not relevant enough to discern if one configuration agrees better than the other. A similar conclusion can be reached analyzing the scatter plots (not shown) comparing the HF radar data with the modeled data at P3. The differences between the *cRS* and *uncR* runs are not relevant, but the modeled cross-shelf components show a better fit with the measurements, with regression slopes of 1.01 for both runs, than the along-shelf components, with regression slopes of 0.64 and 0.68, respectively. In general, the modeled water currents show larger intensities than the measured ones.

Table 3. Statistics comparing the modeled water currents at P3 with data from the HF radar.

		bias	RMSD	r	d
u	*uncS*	-4.20 cm/s	14.02 cm/s	0.56	0.73
	cRS	-1.49 cm/s	13.71 cm/s	0.55	0.74
v	*uncS*	3.50 cm/s	14.18 cm/s	0.65	0.77
	cRS	2.88 cm/s	14.86 cm/s	0.66	0.77

3.2 Description of the ~~wave~~ coupling effects on currents

Fig. 5 compares *uncR* and *cRS* run results during the wind-jet event E3 at P1 (73.7 m depth) and P3 (98.9 m depth) along with HF radar subinertial water surface current at P3. Following Ràfols et al. (2017a), the subinertial currents have been calculated using a tenth order Butterworth filter with a cutoff period of 30 h. The figure also shows the wind intensity evolution at each point and the Hs comparison between the *uncS* and *cRS* run results. The wind-jet event E3 starts on 25 April at 02:00 (UTC), forms very quickly, reaches its maximum intensity at 06:00 and fades gradually. The water current time series show that, during the wind jet peak, ~~there is a negative increase of~~ the cross-shelf current ~~component (~~magnitud increases (it becomes more negative; i.e., it flows offshoreward) and~~a decrease of the along-shelf current. Then, after~~, throughout the wind-jet ~~peak~~event, the along-shelf component becomes more negative (i.e., southwestward). Comparing the results from the *uncR* and *cRS* runs, it is observed that larger differences occur at the shallowest point (P1), with differences up to 20 cm/s, while at P3 both runs present very similar results (with differences lower than 10 cm/s). No measured data are available for P1, thus it cannot be discerned which run best fits the observation. In contrast, at P3, the modeled results can be compared with the HF radar data but it is difficult to state which simulation best reproduces the observations. The influence of waves at the cross-shelf circulation is limited and the surface circulation of both runs presents similar patterns.

With the aim of visualizing the differences in the current patterns and the spatial variability between the different runs, in Fig. 6 the measured HF radar currents are compared with the surface currents obtained with the *uncR* and *cRS* runs in four

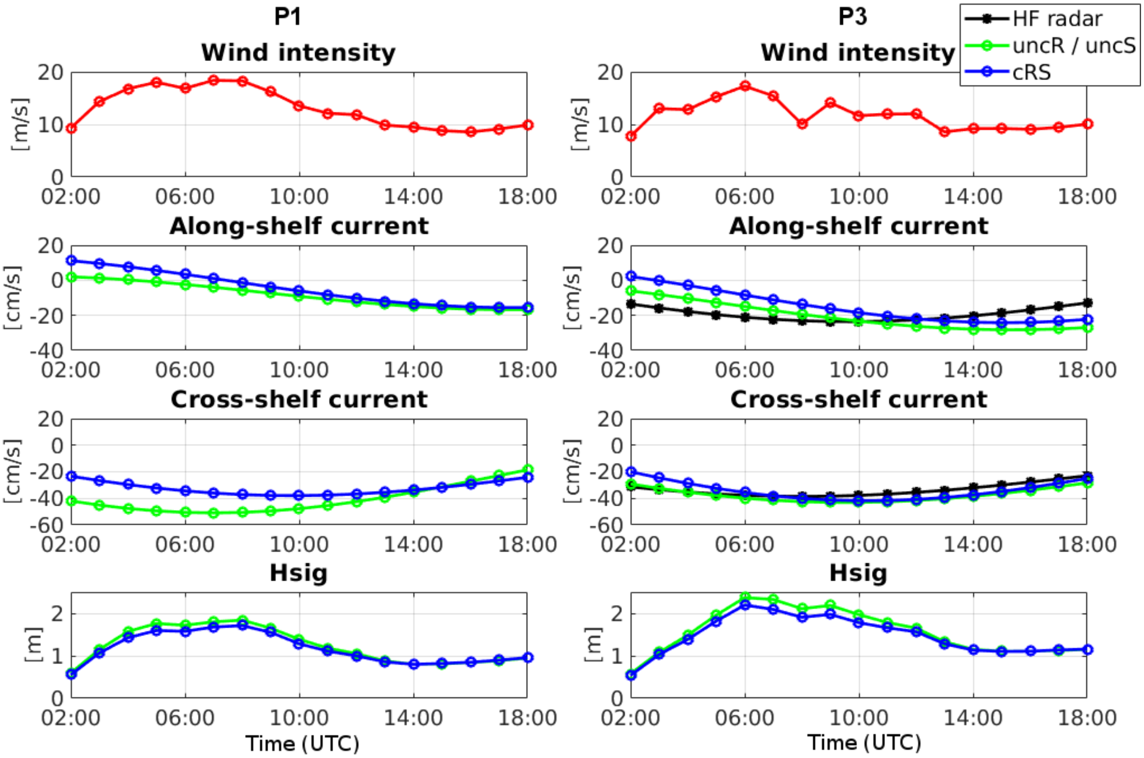

Figure 5. Wind intensity, along- and cross-shelf subinertial surface currents and Hs time series at P1 and P3 during the wind-jet event E3 (25 April 2014). Negative values mean offshore and southwestwards. In red, the modeled wind intensity, in black the HF radar data, in green the *uncR* and *uncS* runs results and in blue the *cRS* run results.

snapshots, which correspond to the evolution of the wind-jet event E3. For clarity, the figure presents the results up to the mid-slope. The modeled water currents are more intense than the water currents measured by the HF radar but the circulation patterns are consistent. There are slight differences between the *uncR* run results and the *cRS* run results. An increase of the current intensity is observed at the start of the wind jet when the waves are considered in the ROMS model (Fig. 6c and 6d second column). In addition, the region affected by the wind jet seems to be expanded to the northeast, resulting in stronger water currents in the cRS run. Nevertheless, the main current patterns obtained with both runs are very similar and coincide with the behavior presented in Ràfols et al. (2017a).

Figure 7 shows the Hs and surface water current mean of the hourly instantaneous differences considering: the whole study period, the whole study period except the wind-jet events and just the four wind-jet events. It is observed that the major differences are obtained during the wind-jet events. The mean differences obtained for the whole period are very similar to the mean differences under no wind-jet conditions, with differences shorter than ±5 cm/s. During wind-jet conditions, a clear decrease of the surface water current intensity is observed at the wind-jet axis when the waves are considered, but the differences are less than 10 cm/s. In contrast, at shallow regions, the surface water current intensities are increased, showing

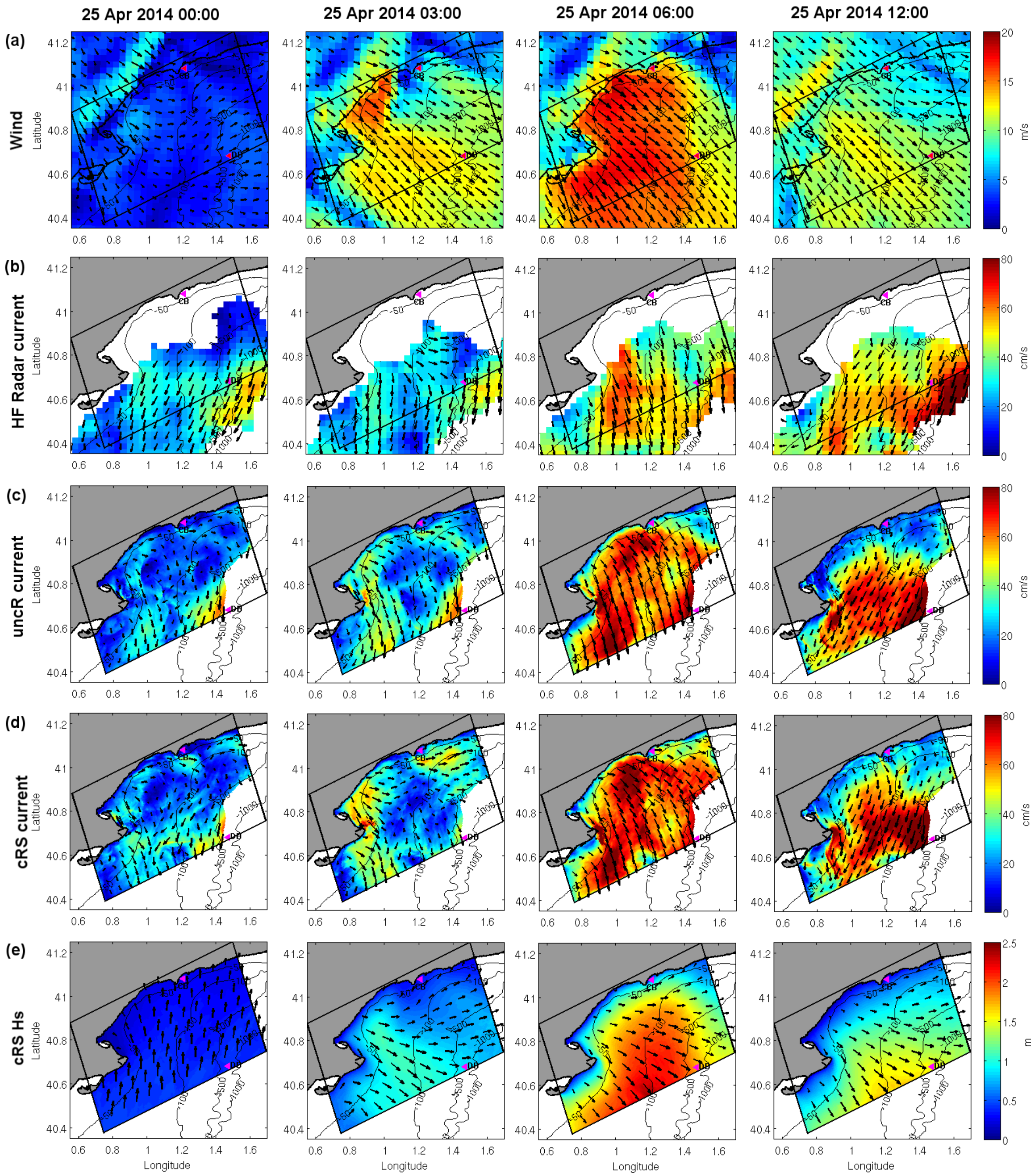

Figure 6. Results for the wind-jet event E3. (a) 10-m wind intensity; (b) HFR current intensity; (c) *uncR*-modeled surface current intensity; (d) *cRS*-modeled surface current intensity; (e) *cRS*-modeled Hs and mean wave direction. For clarity, the results are shown up to the mid-slope. The CB and DB locations are shown with pink triangles.

differences up to 15 – 20 cm/s. An increase of the current intensity is also observed at the northeast corner of the domain but there the differences are just around 5 cm/s.

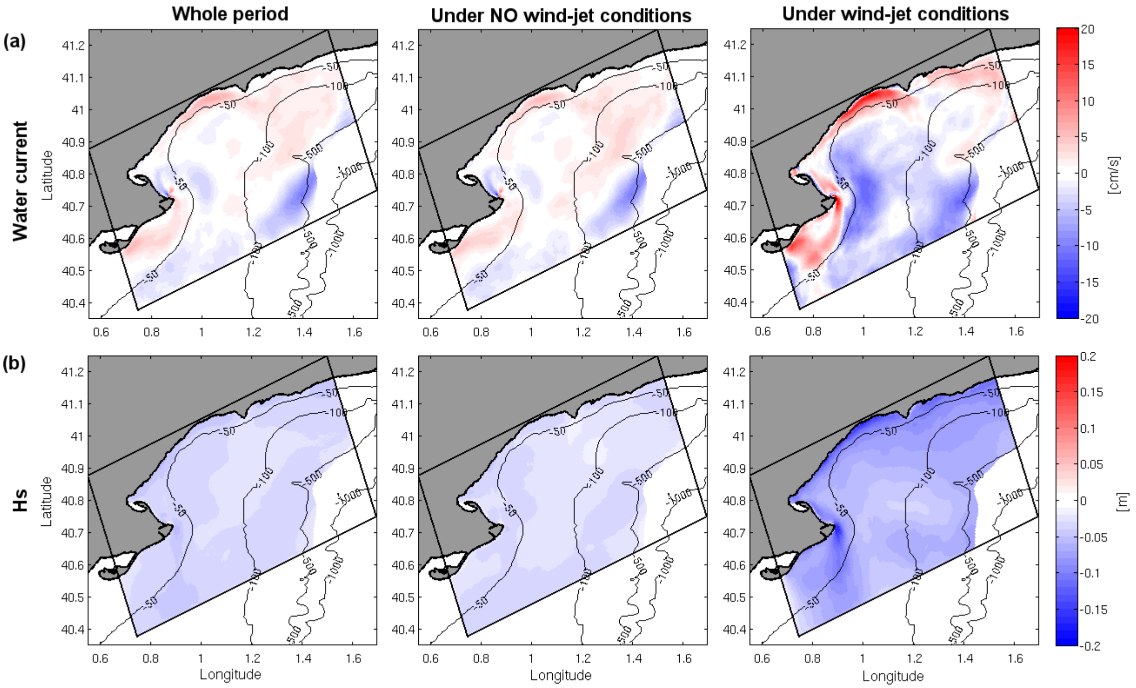

Figure 7. (a) ~~Water~~ Surface water current and (b) Hs mean of the hourly instantaneous differences between the *uncS*/*uncR* run and the *cRS* run considering the whole period (left), the whole period except the wind-jet events (centre) and during the four wind-jet events (right). Positive values correspond to *cRS* value $>$ *uncS*/*uncR* value.

The evolution of the buoyancy or Brunt–Väisälä frequency ($N = \sqrt{-\frac{g}{\rho_0}\frac{\partial \rho(z)}{\partial z}}$, where ρ_0 is the reference density and g is the gravitational acceleration) is investigated in order to analyze the differences between the *uncR* and the *cRS* run results in the water column structure. Figure 8 shows the Brunt–Väisälä frequency evolution (before and after the wind jet) at P3 during the four wind-jet events for both *uncR* and *cRS* runs. It is observed that the vertical structure of the water column is significantly different when the waves are taken into account. The *cRS* run always presents a less stratified water column, both before and after the wind jet. When a wind jet occurs, the expected behavior is that the water column will become less stratified after the wind jet than before it. This is observed in all the studied wind-jet events but the surface mixed-layer depth (SML; i.e. the distance from the surface until the top of the pycnocline) after the wind jet obtained with the *cRS* run is larger (i.e. deeper) than the one obtained by the *uncR* run. Thus, the vertical mixing is significantly enhanced when the waves are taken into account.

Analyzing the results from *uncR* and *cRS* runs, it is found that there is a clear enhancement of the TKE when the waves are considered, also with some increase of the SStr (see Fig. 9). Note that the SStr felt by the ocean is equal to the air-side stress, which in the cRS run include the wave-dependent sea surface roughness, but it does not account for the stress acting on waves and the dissipation due to wave breaking. The mean TKE and SStr values obtained with the model during the wind-jet event

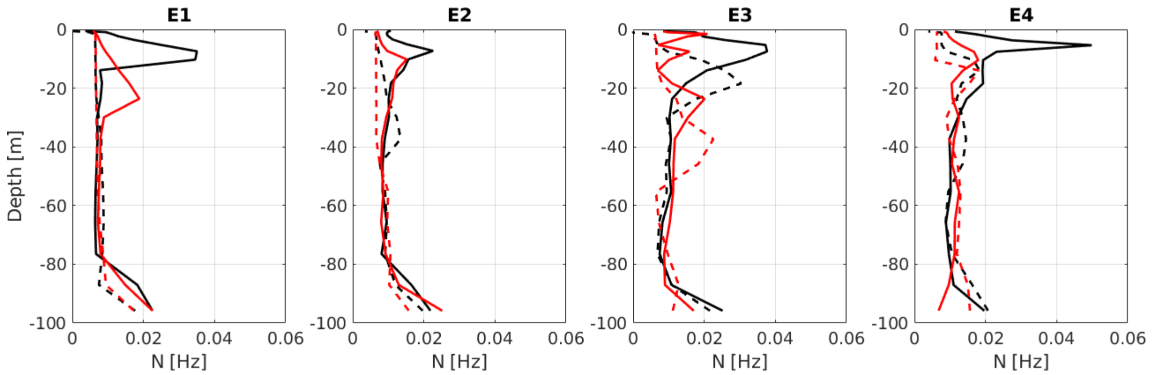

Figure 8. Comparison of the Brunt–Väisälä frequency at the start (solid line) and the end (dashed line) of each wind-jet event obtained from the results of the *uncR* (in black) and *cRS* run (in red) at P3.

E3 at P3 shift from 8.14×10^{-4} m^2/s^2 and 0.25 N/m^2 with the *uncR* run to 5.13×10^{-3} m^2/s^2 and 0.31 N/m^2 with the *cRS* run. Additionally, the TKE and SStr peak coincide with the wind jet peak (25 April at 06:00) and the peak values found at P3 are 2.44×10^{-3} m^2/s^2 and 0.75 N/m^2 for the *uncR* run and 1.11×10^{-2} m^2/s^2 and 0.88 N/m^2 for the *cRS* run. Thus, the TKE is 1 order of magnitude stronger when the waves are considered, which leads to an enhancement of the water column mixing and thus a decrease of the stratification.

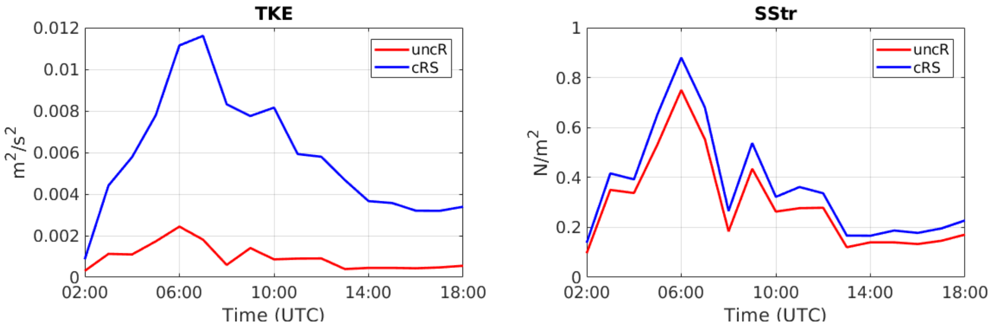

Figure 9. Time series comparison of the TKE (left) and SStr (right) obtained from the results of the *uncR* (in red) and *cRS* run (in blue) at P3 during the wind-jet event E3 (25 April 2014).

In order to evaluate how the waves' effects are taken into account in the momentum balance, the terms of equation 1 are analyzed. During a calm period before the wind jet, the cross-shelf momentum balance is between the *PG* and *COR* terms, and the remaining terms are (at least) 1 order of magnitude smaller. Thus, the ~~wave~~ coupling effects on the momentum balance are negligible. In contrast, during a wind-jet event, more terms are involved in the cross-shelf momentum balance. From the coastline until 4 km offshore ($\sim$50 m depth), the *WF* term (1.85×10^{-5} m/s^2) is on the same order of magnitude as the *PG* (2.42x10^{-5} m/s^2), *SStr* (2.73×10^{-5} m/s^2) and *HA* (1.99×10^{-5} m/s^2) terms. From that point until tens of kilometers offshore the *PG* (1.34×10^{-5} m/s^2) term is mainly balanced by the *SStr* (1.07×10^{-5} m/s^2) and *WF* (5.05×10^{-6} m/s^2) terms, also including some contribution from the *COR* and *HA* terms. However, the *WF* term weight is half the weight of the *SStr* term. Thus, the *WF* term included by the VF formalism plays an important role in the momentum balance in the first kilometers offshore (i.e. in coastal regions). Analyzing the *WF* term, it is found that its main contributor is the surface streaming (B^{sf}; 1.65×10^{-5} m/s^2 and 3.94×10^{-6} m/s^2 for shallow and deep water, respectively), especially in shallow waters, with also some contribution of the wave breaking term (B^b; 2.01×10^{-6} m/s^2 and 1.11×10^{-6} m/s^2,respectively). Regarding the *PG* term, its weight is mainly due to the non-WEC contributions (P^c; 1.60×10^{-5} m/s^2 and 1.37×10^{-5} m/s^2, respectively) together with some contribution of the quasi-static response (P^{qs}; 1.37×10^{-5} m/s^2 and 3.21×10^{-6} m/s^2).

3.3 Description of the ~~current~~ coupling effects on waves

The irregular nature of wind causes irregular wind waves of different heights, periods and directions. For this reason, wind waves are usually described using spectral techniques, where the random motion of the sea surface is treated as a summation of harmonic wave components. In Fig. 10 the wave response during a wind-jet event is analyzed in terms of the variance density spectrum $E(f,\theta)$ evolution obtained from the numerical model. The one- and two-dimensional frequency–direction spectra evolution at P2 (i.e. at the wind-jet axis) obtained with the *uncS* and *cRS* runs during the wind-jet event E3 are compared. The runs show similar spectra evolution patterns. When the wind jet starts, the wave field is adapted to the new wind, generating a bimodal spectrum with a wider peak at the NW (which is consistent with the new wind direction, i.e., it is a new sea system) and a peak at the south corresponding to the "old" sea system. At the peak of the wind jet, the spectra are dominated by the new sea system and, when the wind-jet intensity diminishes, another new sea system occurs, while the energy due to the wind jet decrease gradually. In addition, a swell system appears at the northeast, due to the coexistence of NW wind at the region and northerly wind at the northern part of the coast (Ràfols et al., 2017b). The main difference between the *uncS* and *cRS* runs is that the spectra obtained with the *cRS* run present less energy at the peak than the *uncS* run. An energy increase at higher frequencies (i.e. at the spectrum tail) can also be observed when the currents are considered, but overall the *uncS* run presents more energy. A less energetic spectrum means shorter Hs values, which is consistent with the values obtained from the numerical results.

In Fig. 5 and Fig. 6, it is observed that, during the wind-jet event, the wave field responds directly to the wind. In Fig. 6, the 2D Hs maps show a clear increase of the wave height at the wind-jet axis that, at the wind-jet peak, reaches values up to 2.43 m. The time series presented in Fig. 4 and Fig. 5 show that the Hs diminish when the water currents are considered and that the major differences ($\sim$15–20 cm) occur during the wind-jet peak. Similar results are shown in Fig. 7, where the mean differences show that the Hs from the *cRS* run tend to be shorter than the Hs from the *uncS* run and that the major differences are observed during the wind-jet events. Under such conditions, the mean differences at shallow regions reach values of 15 cm, while the mean difference at the wind-jet axis is around 6 cm. Comparing the results from the *cRS* and the *uncS* runs, it is found that ~~considering the water currents~~ coupling the models produces a mean effect of 11% in the Hs parameter at CB location and a mean effect of 4% at DB location.

In order to analyze the *Hs* differences obtained with the two runs, Fig. 11 shows the differences in *Hs* at P2, distinguishing the differences in the wave and current propagation directions. It is found that the *Hs* from the *cRS* run tends to be shorter (stronger)

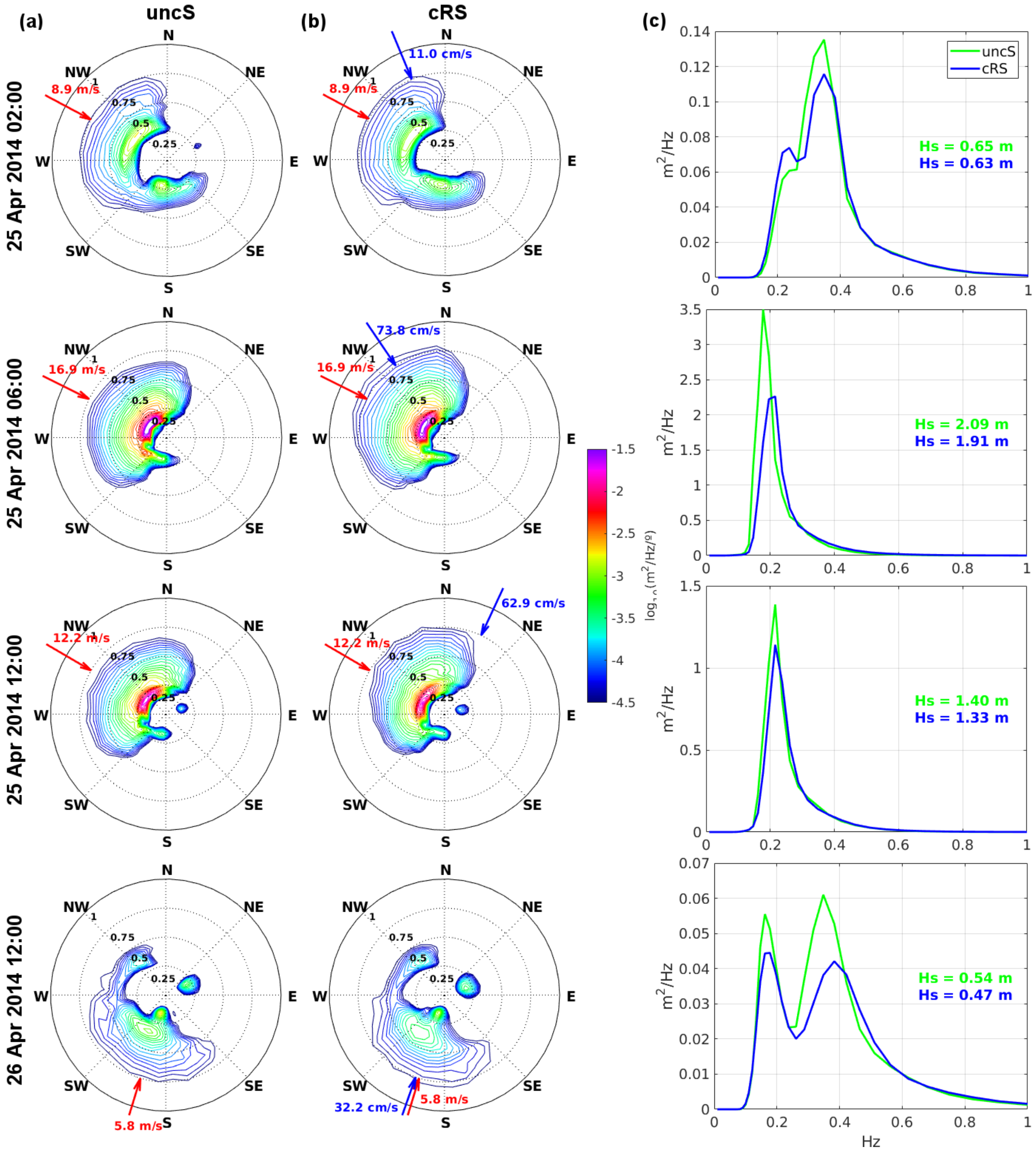

Figure 10. Spectra evolution during event E3 at P2. (a) 2D spectrum from *uncS* run. (b) 2D spectrum from *cRS* run. (c) 1D spectra from both runs and the corresponding Hs values. The arrows shown in a) and b) indicate the direction and magnitude of wind (red) and current (blue).

than the *Hs* from the *uncS* run when the difference between the propagation direction of waves and currents is shorter (stronger). This is to say that ~~including the current effects on waves~~ considering the coupling effects results in a decrease (increase) of *Hs* when the waves and the currents propagate in the same (opposite) direction. In general, the *Hs* differences between the runs are small ($\Delta Hs < 5$ cm). However, during the NW wind jets these differences increase up to 10–14 cm and, in the case of event E3, reach 20 cm. The mean differences observed at this point correspond to 10% of *Hs*.

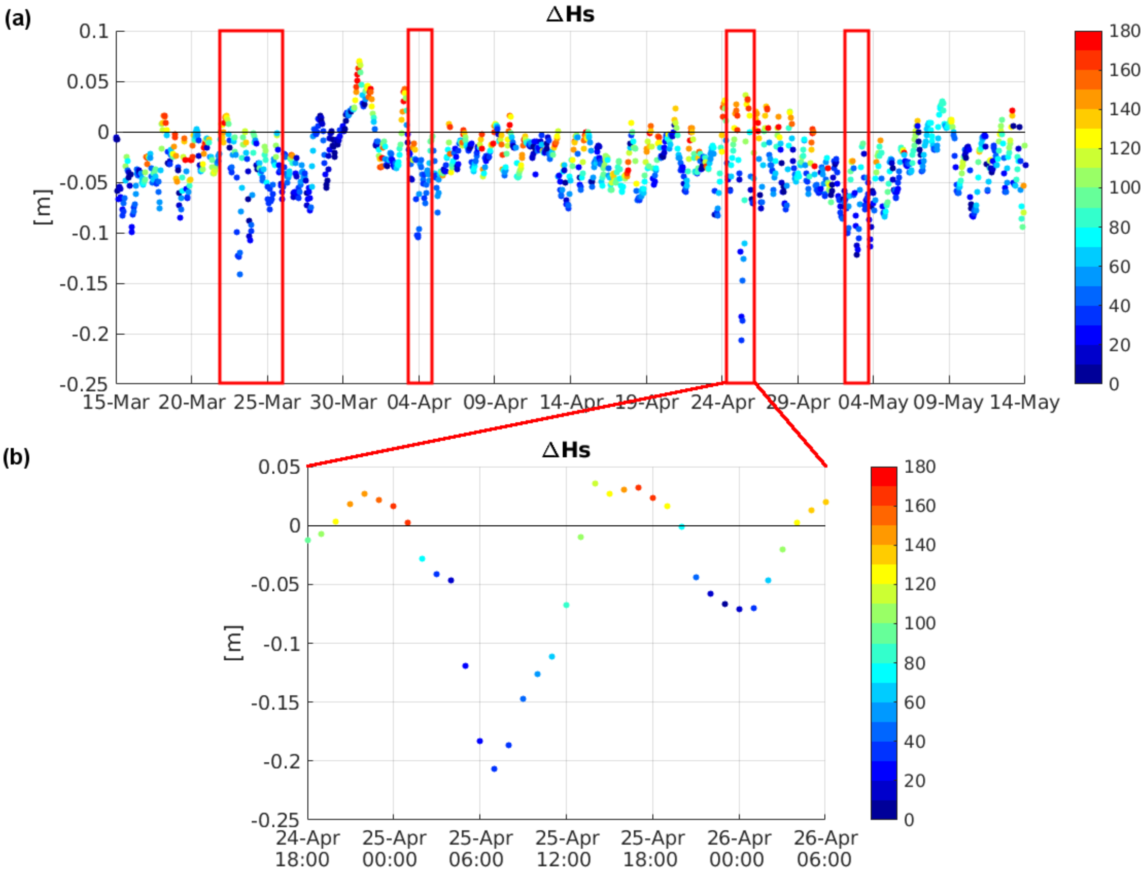

Figure 11. (a) *Hs* differences at P2. The different colors correspond to the angle between the directions of wave and current propagation. (b) Detailed view of the period corresponding to event E3.

The Tm_{02} obtained with the *cRS* tends to be longer than the one obtained with the *uncS* excepting the wind-jet event periods, where the Tm_{02} from the coupled run is shorter (see Fig. 4). This is consistent with the frequency increase in the *cRS* run detected in the spectra analysis during the wind-jet event E3. Figure 12 shows the Tm_{02} and Dir time series obtained with the *uncS* and the *cRS* runs compared to the CB measured data. Note that the CB location is not affected by the wind jet. Qualitatively, the *cRS* run shows a clear improvement in the agreement of the Tm_{02} results with the measurements, which is consistent with the statistical parameters collected in Tables 1 and 2. Comparing the results from the *cRS* and the *uncS* runs, it is found that ~~considering the water currents~~ coupling the models produces an average effect of 48% in the Tm_{02} parameter at the CB location. This effect is reduced to 27% at the DB location.

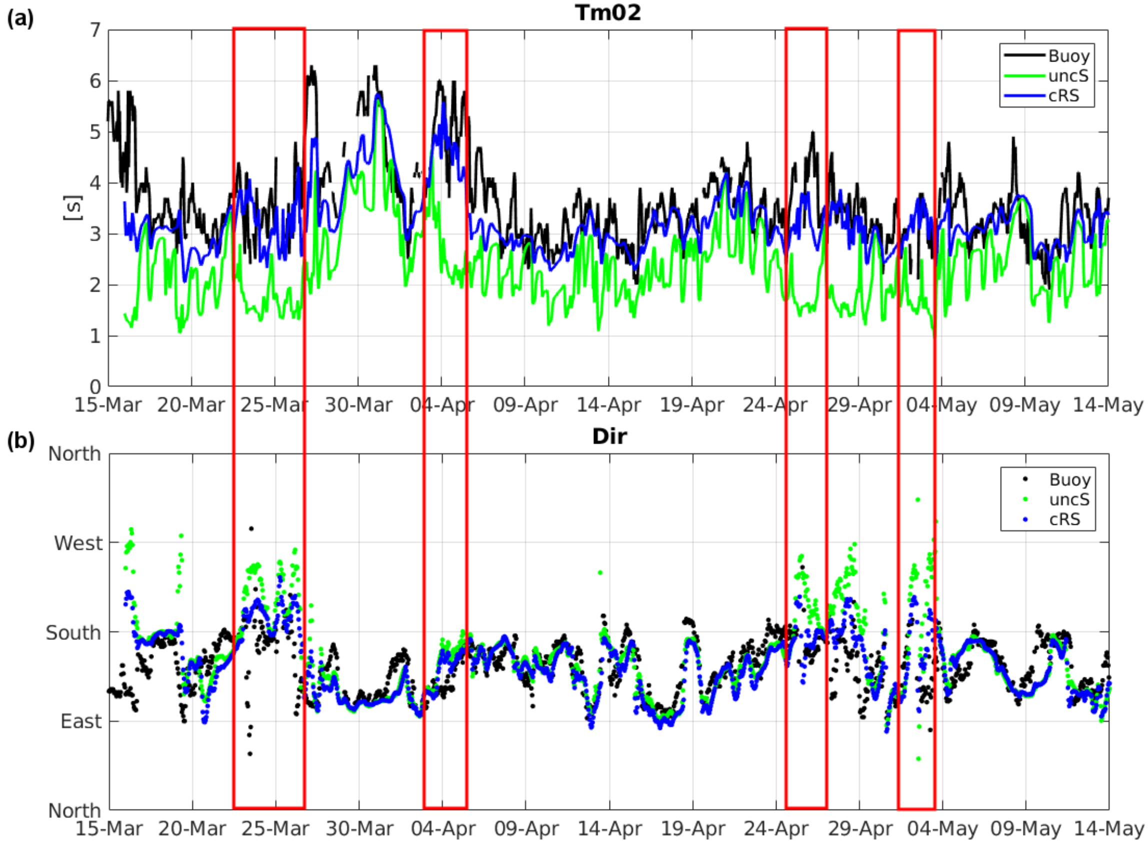

Figure 12. Comparison of the Tm_{02} and Dir parameters time series obtained with the *uncS* (green) and *cRS* (blue) runs with the data measured by CB (black). Note that the first 24 h of the model results have been rejected.

Regarding the mean wave direction, no relevant differences are observed between the *uncS* and *cRS* runs at deep water (not shown). However, similarly to the results presented in Table 2, Fig. 12b shows that at the CB location (i.e. in shallow waters) the mean wave direction is improved during the wind-jet events. Analyzing the mean wave direction differences between the *uncS* and *cRS* runs, it is found that relevant differences occur near the coastline.

5 4 Discussion

4.1 Effects of ~~waves~~ coupling on the current field

The main differences between the *uncR* and *cRS* runs have been detected in the water column structure. The vertical mixing of the water column is stronger when the waves are considered. This behavior can be explained by the TKE injection and the use of a wave-dependent sea surface stress in the *cRS* run. Similar results have been observed in previous work. Rong et al. (2014) studied the WCI over the Texas–Louisiana Shelf and found that the wave effects can redistribute the freshwater both vertically and horizontally and thus affect the stratification. Bruneau and Toumi (2016) also found that the mixed-layer depths were enhanced in presence of waves. Niu and Xia (2017) investigated how the Lake Erie dynamics were impacted by the wave-induced surface stress and found that it produced an enhancement of the surface mixing and a weakening of the stratification strength. It is important to note that, although the results presented in this study are consistent, there are no available measurements to verify them. Thus, it can not be stated if the *cRS* run is more adjusted to the reality or if it is "over-mixing".

The results presented above show that including the wave effects does not produce a relevant difference to the water current velocity during a wind-jet event and has a weak impact on the water circulation patterns. Similar results were presented by Bruneau and Toumi (2016), who analyzed the wave-induced processes at the Caspian Sea and found that they have a weak impact on the dynamics of the region. The momentum balance analysis has shown that the WF term is one of the leading terms in very shallow areas (until ∼50 m water depth). For this reason, using a numerical domain at a more coastal scale with water depths up to 50 m would probably show more effects at the current field, rather than the domain used in this work, which is focused on the inner shelf, where the water depth reaches values higher than 100 m. As a matter of fact, Osuna and Wolf (2005) studied the WCI in the Irish Sea and found that the effect of waves on currents are evident in the eastern coastal areas, with daily mean current differences larger than 10 cm/s during strong wave events.

4.2 ~~Current effects~~ Effects of coupling on the wave field

The numerical results present an improvement in the Tm_{02} parameter when the coupling effects were considered (see Fig. 12a). Consequently, the inclusion of the current velocity in the estimation of wave period is not negligible, and it must be considered if high-quality modeling is required ~~(similar to Bolaños et al. (2014))~~(similar to Bolaños et al., 2014). It should be noted that the results show that the ~~effects of currents~~ coupling effects on the wave field are stronger for the Tm_{02} parameter than for the *Hs* parameter. For instance, Osuna and Monbaliu (2004) found that the effect of coupling is 1 order of magnitude stronger for the Tm_{02} parameter (about 20%) than in the case of *Hs* (about 3%).

During a wind-jet event, a decrease of the *Hs* is found when the currents are taken into account. The decrease (increase) of *Hs* in the presence of an opposite (following) current is a well-known effect that has been investigated before by several authors (e.g. Benetazzo et al., 2013; Dutour Sikirić et al., 2013; Viitak et al., 2016). For example, Benetazzo et al. (2013) studied the WCI at the semi-enclosed Gulf of Venice and found that during Bora conditions, with the currents propagating in the same direction as waves, the comparison between coupled and uncoupled models showed a reduction of *Hs* on the order of 0.6 m when the waves were considered.

The differences in mean wave direction found in shallow waters could be due to the current-induced refraction (Wolf and Prandle, 1999; Olabarrieta et al., 2011). However, it is important to note that these differences were found very near the coastline, specifically until 2 km offshore. Since the model mesh resolution is of 350 m, there are very few grid points and thus it is not possible to extract a concise conclusion about this phenomenon with the results obtained in this study. A study at more coastal scales would be necessary to discern such processes.

Finally, considering the currents causes wave spectral reshaping. During a cross-shelf wind-jet event, the presence of currents induces a shoaling-like process. In general, a reduction of the energy peak and a slight increase of the energy at the tail of the spectrum is observed. This is consistent with the results presented in Fan et al. (2009), where the authors found that when the wave–current interactions were considered, the peak of the frequency spectrum was reduced and shifted toward higher frequency. Rusu (2010) also found that the presence of currents leads to a redistribution of the wave energy over the spectrum.

5 Conclusions and future works

The wave–current interactions have been investigated using numerical models. Three different runs have been performed: an uncoupled ROMS run, an uncoupled SWAN run and a two-way coupled run. The comparison among these runs shows that at the continental shelf the surface water current presents similar results in the coupled and the uncoupled configurations and the momentum balance analysis reveals that the non-conservative wave forcing (WF) term plays an important role in shallow waters. The results show that ~~including wave effects induces~~ coupling the models results in a major mixing of the water column (the SML increase), mainly due to the TKE injection and the enhanced surface stress. Additionally, ~~when the water currents are considered in the waves forecast,~~ wave spectral reshaping occurs, the Tm_{02} improves and the wave energy (and thus the *Hs*) diminishes (increases) when the water currents and waves propagate in the same (opposite) direction. The results also indicate that more processes occur in shallower waters, e.g. current-induced refraction, but a more coastal domain with a finer grid is necessary to evaluate them.

Overall, the numerical results ~~have demonstrated to be~~ are physically reasonable, ~~being capable of reproducing~~ as they reproduce the well known coupling effects. ~~This has allowed to investigate the impact of the WCIs~~ The results have enabled the WCIs to be investigated but more measurements would be needed in order to perform a more quantitative analysis. Thus, in the future it would be interesting to perform some measurement campaigns to enable more accurate model validation and more exhaustive analysis of the dynamics of the region. In addition, it would be interesting to investigate the role of the sea surface roughness coupling the ROMS and SWAN models with the WRF model.

Data availability. HF radar data and buoy measurements used in this contribution can be consulted in http://portus.puertos.es, the IBI-MFC model data is available in http://marine.copernicus.eu and the WRF model data was provided by the Catalan Service of Meteorology (http://meteo.cat/). Data processing and displaying was done using a licensed Matlab program.

Appendix A: The logarithmic wind profile

The logarithmic wind profile used to extrapolate from 10 m to 3 m the modeled wind is as follows

$$U_z = \frac{U^*}{\kappa} \ln\left(\frac{z}{z_0}\right) \tag{A1}$$

where U_z is the mean horizontal wind velocity at a given height z, U^* is the frictional velocity, κ is the von Kármán constant ($\simeq 0.4$) and z_0 is the aerodynamic roughness length.

The roughness length is estimated by means of the Charnock's relation

$$z_0 = \frac{\alpha_{CH} U^{*2}}{g} \tag{A2}$$

where g is the gravitational constant and α_{CH} is the Charnock parameter (in this study it has been considered an α_{CH} equal to 0.011).

The friction velocity is related to the known wind speed at 10 m elevation (U_{10}) with

$$U^{*2} = C_D U_{10}^2 \tag{A3}$$

where C_D is the drag coefficient from Wu (1982)

$$C_D(U_{10}) = \begin{cases} 1.2875 \cdot 10^{-3}, & \text{for } U_{10} < \text{ 7.5 m/s} \\ (0.8 + 0.065 \cdot U_{10}) \cdot 10^{-3}, & \text{for } U_{10} \geq \text{ 7.5 m/s} \end{cases} \tag{A4}$$

Competing interests. The authors declare that they have no conflict of interest.

Acknowledgements. The development of this research was partially funded by the Doctorats Industrials 2013 PhD program of the Catalan Government. The authors also acknowledge Puertos del Estado for the data set provided. This work received funding from the EU H2020 program under grant agreement no. 730030 (CEASELESS project).

References

Benetazzo, A., Carniel, S., Scalvo, M., and Bergamasco, A.: Wave-current interaction: Effect on the wave field in a semi-enclosed basin, Ocean Modelling, 70, 152–165, https://doi.org/10.1016/j.ocemod.2012.12.009, 2013.

Bolaños, R., Osuna, P., Wolf, J., Monbaliu, J., and Sánchez-Arcilla, A.: Development of POLCOMS-WAM model, Ocean Modelling, 36, 102–115, https://doi.org/10.1016/j.ocemod.2010.10.004, 2011.

Bolaños, R., Brown, J., and Souza, A.: Wave-current interactions in a tide dominated estuary, Continental Shelf Research, 87, 109–123, https://doi.org/10.1016/j.csr.2014.05.009, 2014.

Bolaños-Sanchez, R., Sánchez-Arcilla, A., and Cateura, J.: Evaluation of two atmospheric models for wind-wave modelling in the NW Mediterranean, Journal of Marine Systems, 65, 336–353, https://doi.org/10.1016/j.jmarsys.2005.09.014, 2007.

Booij, N., Ris, R., and Holthuijsen, L.: A third-generation wave model for coastal regions - 1. Model description and validation, Journal of Geophysical Research, 104, 7649–7666, https://doi.org/10.1029/98JC02622, 1999.

Bretherton, F. and Garrett, C.: Wavetrains in Inhomogeneous Moving Media, Proceedings of the Royal Society of London. Series A, Mathematical and Physical Sciences, 302, 529–554, http://www.jstor.org/stable/2415989, 1968.

Bruneau, N. and Toumi, R.: A fully-coupled atmosphere-ocean-wave model of the Caspian Sea, Ocean Modelling, 107, 97–111, https://doi.org/10.1016/j.ocemod.2016.10.006, 2016.

Cavaleri, L. and Malanotte-Rizzoli, P.: Wind wave prediction in shallow water: Theory and applications, Journal of Geophysical Research, 86, 961–973, https://doi.org/10.1029/JC086iC11p10961, 1981.

Dutour Sikirić, M., Roland, A., Janeković, I., Tomažić, I., and Zumić, M.: Coupling of the Regional Ocean Modeling System (ROMS) and Wind Wave Model, Ocean Modelling, 72, 59–73, https://doi.org/10.1016/j.ocemod.2013.08.002, 2013.

Fairall, C., Bradley, E., Rogers, D., Edson, J., and Young, G.: Bulk parameterization of air-sea fluxes for tropical ocean-global atmosphere Coupled-Ocean Atmosphere Response Experiment, Journal of Geophysical Research, 101, 3747–3764, https://doi.org/10.1029/95JC03205, 1996.

Fan, Y., Ginis, I., Hara, T., Wright, C., and Walsh, E.: Numerical Simulations and Observations of Surface Wave Fields under an Extreme Tropical Cyclone, Journal of Physical Oceanography, 39, 2097–2116, https://doi.org/10.1175/2009JPO4224.1, 2009.

Font, J., Garcia-Ladona, E., and Gorriz, E.: The seasonality of mesoscale motion in the Northern Current of the western Mediterranean: several years of evidence, Oceanologia Acta, 18, 207–219, http://archimer.ifremer.fr/doc/00096/20772/, 1995.

Grifoll, M., Garcia, V., Aretxabaleta, A., Guillén, J., Espino, M., and Warner, J.: Formation of fine sediment deposit from a flash flood river in the Mediterranean Sea, Journal of Geophysical Research: Oceans, 119, 5837–5853, https://doi.org/10.1002/2014JC010187, 2014.

Grifoll, M., Aretxabaleta, A., and Espino, M.: Shelf response to intense offshore wind, Journal of Geophysical research: Oceans, 120, 6564–6580, https://doi.org/10.1002/2015JC010850, 2015.

Grifoll, M., Navarro, J., Pallares, E., Ràfols, L., Espino, M., and Palomares, A.: Ocean-atmosphere-wave characterisation of a wind jet (Ebro shelf, NW Mediterranean Sea), Nonlinear Processesin Geophysics, 23, 143–158, https://doi.org/10.5194/npg-23-143-2016, 2016.

Haidvogel, D., Arango, H., Budgell, W., Cornuelle, B., Curchitser, E., Lorenzo, E. D., Fennel, K., Geyer, W., Hermann, A., Lanerolle, L., Levin, J., McWilliams, J., Miller, A., Moore, A., Powell, T., Shchepetkin, A., Sherwood, C., Singell, R., Warner, J., and Wilkin, J.: Ocean forecasting in terrain-following coordinates: Formulation and skill assessment of the Regional Ocean Modeling System, Journal of Computational Physics, 227, 3595–3624, https://doi.org/10.1016/j.jcp.2007.06.016, 2008.

Hasselmann, K., Barnett, T., Bouws, E., Carlson, H., Cartwright, D., Enke, K., Ewing, J., Gienapp, H., Hasselmann, D., Kruseman, P., Meerburg, A., Müller, P., Olbers, D., Richter, K., Sell, W., and Walden, H.: Measurements of wind-wave growth and swell decay during the Joint North Sea Wave Project (JONSWAP), Tech. Rep. 12, Deutches Hydrographisches Institut, 1973.

Hasselmann, S., Hasselmann, K., Allender, J., and Branett, T.: Computations and parameterizations of the nonlinear energy transfer in a gravity wave spectrum. Part II: parameterizations of the nonlinear transfer for application in wave models., Journal of Physical Oceanography, 15, 1378–1391, https://doi.org/10.1175/1520-0485(1985)015<1378:CAPOTN>2.0.CO;2, 1985.

Holthuijsen, L.: Waves in Oceanic and Coastal Waters, Cambridge University Press, 2008.

Jacob, R., Larson, J., and Ong, E.: M x N Communication and Parallel Interpolation in CCSM Using the Model Coupling Toolkit, Preprint ANL/MCS-P1225-0205, Mathematics and Computer Science Division, Argonne National Laboratory, 2004.

Jenkins, A.: Wind and wave induced currents in a rotating sea with depth-varying eddy viscosity, Journal of Physical Oceanography, 17, 938–951, https://doi.org/10.1175/1520-0485(1987)017<0938:WAWICI>2.0.CO;2, 1987.

Kirby, J. and Chen, T.-M.: Surface waves on vertically sheared flows: approximate dispersion relations., Journal of Geophysical Research, 94, 1013–1027, 1989.

Komen, G., Hasselmann, S., and Hasselmann, K.: On the existence of a fully developed wind-sea spectrum, Journal of Physical Oceanography, 14, 1271–1285, https://doi.org/10.1175/1520-0485(1984)014<1271:OTEOAF>2.0.CO;2, 1984.

Kumar, N.: Measurement and Three-Dimensional Modeling of Hydrodynamic Processes In the Inner Shelf and Surf Zone, Ph.D. thesis, University of South Carolina, 2013.

Kumar, N., Voulgaris, G., Warner, J., and Olabarrieta, M.: Implementation of the vortex force formalism in the coupled ocean-atmosphere-wave-sediment transport (COAWST) modeling system for inner shelf and surf zone applications, Ocean Modelling, 47, 65–95, https://doi.org/10.1016/j.ocemod.2012.01.003, 2012.

Larson, J., Jacob, R., and Ong, E.: The Model Coupling Toolkit: A New Fortran90 Toolkit for Building Parallel Coupled Models, Preprint ANL/MCS-P1208-1204, Mathematics and Computer Science Division, Argonne National Laboratory, 2004.

Liang, B., Shao, Z., Wu, Y., Shi, H., and Liu, Z.: Numerical study to estimate the wave energy under Wave-Current Interaction in the Qingdao coast, China, Renewable Energy, 101, 845 – 855, https://doi.org/10.1016/j.renene.2016.09.015, 2017.

Lorente, P., Piedracoba, S., Soto-Navarro, J., and Alvarez-Fanjul, E.: Evaluating the surface circulation in the Ebro delta (northeastern Spain) with quality-controlled high-frequency radar measurements, Ocean Science, 11, 921–935, https://doi.org/10.5194/os-11-921-2015, 2015.

Lorente, P., Piedracoba, S., Sotillo, M., Aznar, R., Amo-Balandron, A., Pascual, A., Soto-Navarro, J., and Alvarez-Fanjul, E.: Ocean model skill assessment in the NW Mediterranean using multi-sensor data, Journal of Operational Oceanography, pp. 1–18, https://doi.org/10.1080/1755876X.2016.1215224, 2016.

Madsen, O.: Spectral wave-current bottom boundary layer flows, in: Coastal Engineering 1994, pp. 384–398, Proceedings of the 24th International Conference on Coastal Engineering, Kobe, Japan, 1994.

McWilliams, J., Restrepo, J., and Lane, E.: An asymptotic theory for the interaction of waves and currents in coastal waters, Journal of Fluid Mechanics, 511, 135–178, https://doi.org/10.1017/S0022112004009358, 2004.

Mellor, G.: The three-dimensional current and surface wave equations, Journal of Physical Oceanography, 33, 1978–1989, https://doi.org/10.1175/1520-0485(2003)033<1978:TTCASW>2.0.CO;2, 2003.

Mellor, G.: Some consequences of the three-dimensional current and surface wave equations, Journal of Physical Oceanography, 35, 2291–2298, https://doi.org/10.1175/JPO2794.1, 2005.

Mellor, G.: Reply, Journal of Physical Oceanography, 41, 2013–2015, https://doi.org/10.1175/JPO-D-11-071.1, 2011.

Millot, C.: Circulation in the Western Mediterranean Sea, Journal of Marine Systems, 20, 423–442, https://doi.org/10.1016/S0924-7963(98)00078-5, 1999.

Niu, Q. and Xia, M.: The role of wave-current interaction in Lake Erie's seasonal and episodic dynamics, Journal of Geophysical Research: Oceans, 122, 7291–7311, https://doi.org/10.1002/2017JC012934, 2017.

O'Donncha, F., Hartnett, M., Nash, S., Ren, L., and Ragnoli, E.: Characterizing observed circulation patterns within a bay using HF radar and numerical model simulations, Journal of Marine Systems, 142, 96–110, https://doi.org/10.1016/j.jmarsys.2014.10.004, 2015.

Olabarrieta, M., Warner, J., and Kumar, N.: Wave-current interaction in Willapa Bay, Journal of Geophysical Research, 116, https://doi.org/10.1029/2011JC007387, 2011.

Osuna, P. and Monbaliu, J.: Wave-current interaction in the Southern North Sea, Journal of Marine Systems, 52, 65–87, https://doi.org/10.1016/j.jmarsys.2004.03.002, 2004.

Osuna, P. and Wolf, J.: A numerical study on the effect of wave-current interaction processes in the hydrodynamics of the Irish Sea, in: Ocean Wave Measurement and Analysis, Fifth International Symposium WAVES, Madrid, Spain, paper number: 93, 2005.

Port, A., Gurgel, K., and Staneva, J.: Tidal and wind-driven surface currents in the German Bight: HFR observations versus model simulations, Ocean Dynamics, 61, 1567–1585, https://doi.org/0.1007/s10236-011-0412-9, 2011.

Ràfols, L., Grifoll, M., Jordà, G., Espino, M., Sairouní, A., and Bravo, M.: Shelf circulation induced by an orographic wind jet, Journal of Geophysical Research: Oceans, 122, 8225–8245, https://doi.org/10.1002/2017JC012773, 2017a.

Ràfols, L., Pallares, E., Espino, M., Grifoll, M., Sánchez-Arcilla, A., Bravo, M., and Sairouní, A.: Wind-Wave Characterization in a Wind-Jet Region: The Ebro Delta Case, Journal of Marine Science and Engineering, 5, https://doi.org/10.3390/jmse5010012, 2017b.

Renault, L., Chiggiato, J., Warner, J., Gomez, M., Vizoso, G., and Tintoré, J.: Coupled atmosphere-ocean-wave simulations of a storm event over the Gulf of Lion and Balearic Sea, Journal of Geophysical Research, 117, https://doi.org/10.1029/2012JC007924, 2012.

Rong, Z., Hetland, R., Zhang, W., and Zhang, X.: Current-wave interaction in the Mississippi-Atchafalaya river plume on the Texas-Louisiana shelf, Ocean Modelling, 84, 67–83, https://doi.org/10.1016/j.ocemod.2014.09.008, 2014.

Rusu, E.: Modelling of wave-current interactions at the mouths of the Danube, Journal of Marine Science Technology, 15, 143–159, https://doi.org/10.1007/s00773-009-0078-x, 2010.

Sánchez-Arcilla, A., González-Marco, D., and Bolaños, R.: A review of wave climate and prediction along the Spanish Mediterranean coast, Natural Hazards and Earth System Sciences, 8, 1217–1228, https://doi.org/10.5194/nhess-8-1217-2008, 2008.

Shchepetkin, A. and McWilliams, J.: The regional oceanic modeling system (ROMS): a split-explicit, free-surface, topography-following-coordinate oceanic model, Ocean Modelling, 9, 347–404, https://doi.org/10.1016/j.ocemod.2004.08.002, 2005.

Sheng, Y., Zhang, Y., and Paramygin, V.: Simulation of storm surge, wave, and coastal inundation in the Northeastern Gulf of Mexico region during Hurricane Ivan in 2004, Ocean Modelling, 35, 314 – 331, https://doi.org/10.1016/j.ocemod.2010.09.004, 2010.

Svendsen, I.: Wave heights and set-up in a surf zone, Coastal Engineering, 8, 303–329, https://doi.org/10.1016/0378-3839(84)90028-0, 1984.

Svendsen, I., Haas, K., and Zhao, Q.: Quasi-3D nearshore circulation model SHORECIRC, Center for Applied Coastal Researc, Department of Civil Engineering, University of Delaware, Newark, user's Manual, Draft Report, 2002.

Tang, C., Perrie, W., Jenkins, A., DeTracey, B., Hu, Y., Toulany, B., and Smith, P.: Observation and modeling of surface currents on the Grand Banks: a study of the wave effects on surface currents, Journal of Geophysical Research, 112, https://doi.org/10.1029/2006JC004028, 2007.

Taylor, P. and Yelland, M.: The dependence of sea surface roughness on the height and steepness of the waves, Journal of Physical Oceanography, 31, 572–590, https://doi.org/10.1175/1520-0485(2001)031<0572:TDOSSR>2.0.CO;2, 2001.

Uchiyama, Y., McWilliams, J., and Schepetkin, A.: Wave-current interaction in an oceanic circulation model with a vortex-force formalism: Application to the surf zone, Ocean Modelling, 34, 16–35, https://doi.org/10.1016/j.ocemod.2010.04.002, 2010.

Viitak, M., Maljutenko, I., Alari, V., Suursaar, Ü., Rikka, S., and Lagemaa, P.: The impact of surface currents and sea level on the wave field evolution during St. Jude storm in the eastern Baltic Sea, Oceanologia, 58, 176–186, https://doi.org/10.1016/j.oceano.2016.01.004, 2016.

Warner, J., Sherwood, C., Arango, H., and Signell, R.: Performance of four turbulence clousure methods implemented using a generic length scale method, Ocean Modelling, 8, 81–113, https://doi.org/10.1016/j.ocemod.2003.12.003, 2005.

Warner, J., Perlin, N., and Skyllingstad, E.: Using the Model Coupling Toolkit to couple earth system models, Environmental Modelling and Software, 23, 1240–1249, https://doi.org/10.1016/j.envsoft.2008.03.002, 2008a.

Warner, J., Sherwood, C., Signell, R., Harris, C., and Arango, H.: Development of a three-dimensional, regional, coupled wave, current, and sediment-transport model, Computers and Geosciences, 34, 1284–1306, https://doi.org/10.1016/j.cageo.2008.02.012, 2008b.

Warner, J., Armstrong, B., He, R., and Zambon, J.: Development of a Coupled Ocean-Atmosphere-Wave-Sediment Transport (COAWST) Modeling System, Ocean Modelling, 35, 230–244, https://doi.org/10.1016/j.ocemod.2010.07.010, 2010.

Willmott, C.: On the validation of models, Physical Geography, 2, 184–194, https://www.tandfonline.com/doi/abs/10.1080/02723646.1981.10642213, 1981.

Wolf, J. and Prandle, D.: Some observations of wave-current interaction, Coastal Engineering, 37, 471–485, https://doi.org/10.1016/S0378-3839(99)00039-3, 1999.

Wu, J.: Wind-stress coefficients over sea surface from breeze to hurricane, Journal of Geophysical Research, 87, 9704–9706, https://doi.org/10.1029/JC087iC12p09704, 1982.

Xie, L., Wu, K., Pietrafesa, L., and Zhang, C.: A numerical study of wave-current interaction through surface and bottom stresses: Wind-driven circulation in the South Atlantic Bight under uniform winds, Journal of Geophysical Research, 106, 16 841–16 855, https://doi.org/10.1029/2000JC000292, 2001.

Xie, L., Liu, H., and Peng, M.: The effect of wave-current interactions on the storm surge and inundation in Charleston Harbor during Hurricane Hugo 1989, Ocean Modelling, 20, 252 – 269, https://doi.org/10.1016/j.ocemod.2007.10.001, 2008.